HER2 Cellular Localization, Cell-Cell Contacts, and Cell Density Regulate Cancer Cell Plasticity in HER2+ Breast Cancer

Saba Sameri[1], Durdam Das[2], Shabnam Shahrivari[1], Vladan Milosevic[3], Shamim Sarhadi[4], Huiqin Koerkel-Qu[1], Carolina Fisch[1], Miriam Kokal[1], Michael Schletter[5], Paul S. Hahn[1], Lisa Seider[6], Marisa Schübel[1], Stefanie Michaelis[7], Joachim Wegener[7,8], Florian Weber[9], Martin Hoffmann[2], Christian Werno[2], Kathrin Weidele[2], Astrid Bruckmann[10], Arne Östman[3], Ernst R. Tamm[11], Yuting Li[12], Christoph A. Klein[1,2], Hedayatollah Hosseini[1]

1 Experimental Medicine and Therapy Research, University of Regensburg, Germany
2 Fraunhofer Institute for Toxicology and Experimental Medicine ITEM, Regensburg, Germany
3 Centre for Cancer Biomarkers CCBIO, Department of Clinical Medicine, University of Bergen, Norway
4 Institute of Clinical Chemistry and Pathobiochemistry, Technical University of Munich, Germany
5 Department of Medicine– Hematology/Oncology, University Hospital Erlangen, Germany
6 Department of Evolutionary Developmental Biology, Institute of Zoology, University Innsbruck, Austria
7 Fraunhofer Institute for Electronic Microsystems and Solid State Technologies EMFT, Regensburg, Germany
8 Institute of Analytical Chemistry, University of Regensburg, Germany
9 Institute of Pathology, University of Regensburg, Germany
10 Institute for Biochemistry, Genetics and Microbiology (Biochemistry I), University of Regensburg, Germany
11 Department of Human Anatomy and Embryology University of Regensburg, Germany
12 Wuya College of Innovation, Shenyang Pharmaceutical University, ShenYang, China

Abstract:

Phenotypic plasticity in HER2+ breast cancer presents a significant challenge in comprehending and treating early-stage metastasis. We conducted an extensive study employing *in vitro* models and patient samples to investigate the relationships among cell density, HER2 expression, HER2 cellular localization, and their impact on the plasticity program of HER2+ breast cancer cells.

Our research reveals a previously unexplored facet of HER2+ breast cancer biology. In conditions of low cellular density, the endoplasmic reticulum (ER) undergoes a remarkable transformation, shifting its function from protein trafficking to serving as a regulator of calcium flux via the PLC pathway. This alteration in ER function leads to the accumulation of HER2 protein within the perinuclear ER compartment.

Furthermore, we discovered that in situations of low cellular density or loss of cell-cell contact among epithelial cells, an epithelial-to-mesenchymal transition (EMT) program is activated, resulting in a significant upregulation of desmosome junctions. Desmosome junctions persist as the longest-lasting epithelial cell junctions on the cell surface and represent the primary means for solitary epithelial cells to establish initial contact. Notably, our research revealed a physical binding between HER2 and Desmoplakin (DSP), facilitating HER2 membrane localization upon early cell-cell contact that initiates the proliferation of cancer cells. The switching from migration to proliferation hinges on a competition between the HER2 membrane pathway and the PLC pathway for the shared target molecule, PIP2. Upon HER2 membrane localization, the PI3K pathway is activated, converting PIP2 to PIP3. Simultaneously, HER2 activation upregulates PDPK1, whose PH domain exhibits a high binding affinity to PIP2 molecules. Consequently, membrane localization of HER2 substantially diminishes PIP2 availability for the PLC pathway, redirecting cells toward proliferation. Analysis of patient samples confirms the loss of membrane bound HER2 in circulating tumor cells (CTCs) and highlights phenotypic transitions in solitary cancer cells. These cells are characterized by increased plakoglobin, elevated ZEB1, and reduced KI67 protein levels.

In summary, our findings introduce a novel mechanism of phenotypic plasticity in HER2+ breast cancer that regulates phenotype switching. This mechanism holds promise for the interception of early-stage metastasis, potentially leading to improved outcomes for HER2+ breast cancer patients.

Keywords: HER2, phenotypic plasticity, desmosome junctions, PDPK1, breast cancer, metastasis.

Introduction

In recent years, a growing body of research has illuminated the concept of early cancer dissemination, challenging traditional notions of metastasis (*1, 2*). This paradigm shift underscores the notion that cancer cells may disseminate at an earlier stage, co-evolving alongside primary tumors and eventually giving rise to metastases. This shift has raised a pivotal question: How can we shift our focus toward preventing metastasis when we lack drugs specifically targeting Disseminated Tumor Cells (DTCs) or Circulating Tumor Cells (CTCs) (*1*).

To answer this question effectively, a comprehensive understanding of the biology of cancer dissemination and the molecular mechanisms governing cancer cell dissemination and early colonization is essential. Our previous research into the BALB-neuT murine model has shed light on this matter. We observed a strong correlation between the expression level of the HER2 oncoprotein, cellular density, and cancer cell migration, dissemination, and proliferation capabilities (*3, 4*). Notably, lower HER2 expression in low-density cancer cell lines or early BALB-neuT lesions correlated with increased migration and sphere formation abilities. Conversely, HER2 upregulation and high cellular density was associated with a higher proliferation rate in advanced tumors (*3, 4*).

Traditionally, the Epithelial-Mesenchymal Transition (EMT) and Mesenchymal-Epithelial Transition (MET) program has been the focal point of discussions on cancer cell plasticity (*5*). However, recent studies have highlighted the role of cell density in regulating epithelial cell migration and proliferation abilities (*6-8*). This aspect had been previously overlooked by classical EMT regulators. During EMT, changes in the expression of genes encoding adhesion molecules impact cell-cell and cell-ECM interactions (*9*). Remarkably, even without external EMT inducers, cell density induces the loss of cell-cell adhesion in epithelial cells, leading to increased motility (*10*) inducing EMT program (*11*) and enhancing the potential for vascular invasion (*3, 4*).

While HER2 overexpression in breast cancer cells is known to promote proliferation (*12*), limited knowledge exists regarding the correlation between oncogene expression levels and different cancer cell phenotypes. Notably, three independent studies consistently reported that robust activation of oncogenic pathways, including c-Myc overexpression in human metastatic breast cancer cells(*13*), simultaneous activation of Akt-1 and HER2 in HER2 murine breast cancer cells (*14*) and activation of K-Ras in the intestinal adenocarcinoma mouse model (APC-/- /K-Ras wt/mut(V12))(*15*), leads to increased proliferation while reducing cancer motility and metastatic ability. These findings beside other cumulative reports suggest that cancer cell dissemination, a critical facet of metastasis, may necessitate a transition from a proliferative to an invasive state(*16*).

HER2, a key oncogene driving 20% of breast cancers, known as HER2 subtypes(*17*), also plays a pivotal role in the progression of other breast cancer subtypes (*18-20*), as well as ovarian and cervical cancers (*21*) and gastric cancer(*22*). This underscores its essential role and potential as a target for cancer therapies. Another intriguing observation about HER2 is the non-membrane staining of HER2 protein in breast cancer as well as other cancer types and its correlation with worse clinical outcomes (*19, 21, 22*). Furthermore, studies have demonstrated that HER2 mRNA or protein levels, are markedly dysregulated in disseminated cancer cells in breast cancer patients with positive HER2 status of their primary tumors (*23-26*).

In light of these observations, we postulate the existence of a plasticity mechanism regulating cancer cell phenotypic switches at the time of dissemination and colonization. This mechanism

involves cancer cell density, HER2 expression, and the cellular localization of HER2—topics we aim to investigate in this study.

In this investigation, we employ a combination of *in vitro* modeling to manipulate HER2 expression levels and vary cell density conditions. This approach allows us to delve into the regulation of cancer cell phenotypic transitions based on the cellular localization of HER2. Under low-density (LD) conditions, alterations in endoplasmic reticulum (ER) function, specifically related to protein trafficking and calcium flux via the PLC pathway, lead to HER2 accumulation within ER compartments, hindering cell proliferation. As early cell-cell contact is initiated, primarily mediated by desmosome junctions, the DSP protein, with a physical binding to HER2 proteins, localizes to the cell membrane, subsequently triggering cell proliferation. The activation of the HER2 pathway involves the utilization and occupancy of PIP2 molecules, which, in turn, inhibits the PLC pathway, suppressing the migration properties of cancer cells. These findings, in conjunction with patient data, present compelling evidence for a novel cancer cell plasticity mechanism within breast cancer, elucidating the dynamics of phenotypic transitions in disseminated cancer cells.

Results

Cell density state, HER2 expression level, and HER2 cellular localization are correlated to the cancer cell phenotypic switch:

In our prior investigation utilizing the BALB-neuT breast cancer model, a significant disparity in dissemination ability was observed between early lesion (EL) cells and primary tumor (PT) cells (*3*). EL cells demonstrated a notably higher capacity for dissemination compared to PT cells. Conversely, PT cells exhibited elevated proliferative rates. Subsequent experiments were conducted, encompassing primary lesions from the BALB-neuT mouse model and human HER2+ (HER2 IHC scores +1, +2, and +3) breast PT samples. These investigations revealed a distinctive pattern: solitary cancer cells which were found to be detached from the epithelial structures and detected by cytokeratin staining (CK8/18), exhibited non-membrane HER2 staining (Figures 1A-B). Further investigation included an *in vitro* invasion assay utilizing a Boyden chamber coated with 40% matrigel. Cells isolated from EL lesions of BALB-neuT mice were seeded at a density of 50,000 cells per 24 well inserts, with FCS-free medium above and FCS-containing medium below the chamber. Notably, the *in vitro* invasion assay revealed migrating cells on the opposite side of the Boyden chamber's membrane, with HER2 staining notably absent from the cell membrane. Instead, HER2 was exclusively localized to the cell-cell contact surface (Figure 1C).

Building upon our previously reported findings, which demonstrated that EL cells disseminate more than PT cells, we hypothesized that the number of cell-cell contacts and cancer cell density might be associated with the higher proliferation rates observed in PT cells as compared to EL lesions. Our cytokeratin (CK8/18) staining supported this hypothesis, as it indicated that cells within PT lesions formed denser epithelial structures in both murine (Figures 1D and E) and human samples (Figures S1A and B). Notably, cells within these dense structures exhibited more pronounced proliferative features in Ki67 staining in both murine (Figure 1F) and human samples (Figure S1C).

Subsequently, we examined the membrane localization of HER2 in breast cancer cells in relation to varying cancer cell densities. To accomplish this, we selected various cell lines with different HER2-expression profiles (Figure S1D) and evaluated HER2 localization under different cell culture density conditions. Our results demonstrated that in cell lines with low to moderate HER2 expression

levels (e.g., MCF7 and T47D for human cell lines, and 4T1 and TUBO for murine cell lines; 72 hours culturing), HER2 was localized to the cytoplasmic-nuclear compartment at low cellular densities (500 cells/cm^2) but localized to the cell membrane at high cellular densities (20000 cells/cm^2) (Figures 1G and S1E). Immunoblotting for the cytoplasmic and nuclear fractions of MCF7 cells under low and high-density conditions was also performed to validate the presence of HER2 in the nuclear fraction of cells cultured at low-density conditions (Figures S1F). However, cellular localization of HER2 was not observed in low density for cell lines with strong HER2 expression (e.g., MDA-MB453, SKBR3; 72 hours culturing) (Figures 1H and S1G).

In summary, these results collectively suggest the presence of a cancer cell plasticity mechanism, which involves cell-cell contact, cell density, and HER2 expression levels. This mechanism plays a pivotal role in regulating HER2 cellular localization and influencing the phenotypic switch in cancer cell migration and proliferation.

HER2 expression level and cell density regulates plasticity program of mammary and breast cancer cells:

Investigating changes in HER2 cellular localization under varying cell densities, which subsequently led to distinct cell phenotypes, prompted our exploration into the impact of HER2 expression on localization and phenotypic transitions. To address this, we established a Tet-On HER2 inducible model incorporating an eGFP tag for tracking HER2 expression and cellular localization in MCF10A cells, denoted as MCF10A-Teti-HER2_GFP (Figure S2A). In this model, Doxycycline (Dox), a stable derivative of Tetracycline, induces HER2 expression, which is trackable through GFP. By modulating HER2 expression levels at different cell densities, we observed that HER2 localizes to the cell membrane at high density (HD) and around the nucleus at low density (LD) (Figure 2A and B). Furthermore, we assessed HER2 and eGFP mRNA levels through quantitative PCR (qPCR), confirming the model's dose-dependent response to Dox (Figure S2B and C). Subsequently, we conducted immunoblotting of cytoplasmic and nuclear fractions from MCF10A-Teti-HER2_GFP cells treated with 1 µM Dox under HD and LD conditions for 72 hours. These analyses revealed higher HER2 expression in the LD nuclear fraction relative to the HD condition, aligning with findings from immunoblotting in MCF7 cells (Figure S1D) (Figure 2C).

Inducing HER2 expression in MCF10A-Teti-HER2_GFP cells under LD conditions notably enhanced the cell proliferation pathway, evidenced by elevated levels of p-AKT, p-PDPK1, and p-ERK in immunoblotting, increased cell counts, and XTT assay results (Figure 2D-E and S2D). Conversely, upregulating the cell proliferation pathway by increasing HER2 expression resulted in decreased migration ability of MCF10A-Teti-HER2_GFP cells, as demonstrated in cell motility assays (Figure 2G). These phenotypic transitions were further evidenced by altered expression levels of migration and proliferation markers at constant HER2 expression (1 µM Dox) under different cell densities, including reduced Ki67 and PCNA expression but increased MMP9, MMP14, and FN1 levels in LD (Figure S2E).

Moreover, HER2 membrane localization of MCF10A-Teti-HER2_GFP cells increased with elevated HER2 expression by Dox treatment after 72 hours culturing (Figure 2H), consistent with findings in the MCF7 cell line, where increased cell density increased HER2 membrane localization (Figure S2F).

To confirm that these results were not influenced by the eGFP tag on HER2, we generated a non-GFP tagged MCF10A-Teti-HER2 model, which corroborated our primary findings from the MCF10A-Teti-HER2_GFP model, thus strengthening our results (Figure S2G-K).

Observing reduced cell motility and induced cell proliferation with increased HER2 expression and cell density, we postulated that HER2 expression level and cell density might jointly regulate the epithelial-mesenchymal transition (EMT) state of these cells. To investigate this, we examined the EMT profile of MCF10A-Teti-HER2_GFP cells under different Dox concentrations (72 hours of culturing). Interestingly, we found that increasing HER2 expression and cell density reduced the mesenchymal state of cells (Figure 2I and J).

To ascertain whether the reduction of the mesenchymal state resulted solely from increased cell density induced by HER2 expression (Figure 2F-I) or if HER2 expression level played a role, we treated MCF10A-Teti-HER2_GFP cells in LD conditions with Dox and/or TGF-β as classical inducer of mesenchymal phenotype. Our findings indicated that TGF-β (TGF- β1, 5 ng/ml; refreshing every 24 hours for three days), treatment in low density conditions induced a pronounced mesenchymal phenotype. Co-treatment of cells with TGF-β and Dox revealed that the mesenchymal state of cells remained stable (Figure 2K). This experiment clarified that HER2 expression level alone does not regulate the mesenchymal state of cells. To investigate the impact of cell density alone on the regulation of the mesenchymal state of cells, we cultured MCF10A-Teti-HER2_GFP cells at constant HER2 expression (1 µM Dox) in LD conditions and tracked the phenotypic traits over extended culturing periods. Remarkably, cell density primarily governed the mesenchymal phenotype of cells, with this effect becoming more pronounced after 15 days compared to 3 days of culturing in low density conditions (Figure 2L). Comparable results were observed for other human breast cancer cell lines including HCC-1806, MCF7 and T47D (Figure S2L).

In summary, these results underscore the pivotal roles played by HER2 expression level and cell density in governing HER2 cellular localization and contributing to phenotypic switch in cancer cells.

Desmosome junctions initiate HER2 membrane localization in the early cell-cell contacts:

Our investigation has shed light on the pivotal role of HER2 cellular localization in orchestrating cancer cell phenotypes. We have revealed that cell density and cell-cell contact are fundamental factors affecting the cellular localization of HER2. To delve deeper into the involvement of cell junctions in this process, we conducted a comprehensive series of experiments and investigations.

Initially, we observed that when MCF10A-Teti-HER2_GFP cells were treated with 1 µM Dox and cultured in high-density (HD) conditions with cell-cell contact, a distinct membrane localization of HER2 emerged at the cell-cell contact surface (Figure 3A). This intriguing observation led us to formulate a hypothesis that cell-cell contact might play a crucial role in the membrane localization and stabilization of HER2. To further investigate this hypothesis, we meticulously examined the HER2 cellular position in solitary cells derived from 32 primary tumor samples of HER2+ breast cancer cells (HER2 IHC scores 1+, 2+, 3+). Remarkably, our analysis revealed a direct correlation between the number of cell contacts and HER2 membrane localization in these cells (Figure 3B).

In a separate experiment, we subjected SKBR3 cells to a non-adherent condition using ultra-low adherent culturing plates and inhibited cluster formation by employing shaking incubators (70rpm). Remarkably, after 48 hours, we made the striking observation that HER2 had disappeared from the cell membrane, underscoring the pivotal role of cell junctions in stabilizing membrane-bound HER2 (Figure 3C-D). Interestingly, reducing cell-membrane HER2 was sufficient to restore the cellular localization of HER2, a phenomenon not previously observed in strongly HER2-expressing cells. Our quantification results, which correlate the HER2 staining signal with DAPI as a nuclear staining indicator, demonstrated a strong correlation between these two staining signals in the nuclear and endoplasmic (NER) regions of SKBR3 cells only 6 hours after seeding for cells that had undergone 48 hours of contact inhibition (Figure 3E). In line with the concept of non-membrane HER2 triggering a phenotypic change, cytoplasmic localization of HER2 in SKBR3 cells led to a reduction in their proliferation ability, as indicated by Ki67 staining results (Figure S3A).

To explore potential protein binding partners involved in HER2 cellular localization, we conducted immunoprecipitation experiments under both low-density (LD) and HD conditions. We utilized MCF10A-Teti-HER2_GFP cells treated with 1 µM Dox and SKBR3 cells (for SKBR3 LD cells, cells were collected 6 hours culturing of cells undergo cell contact inhibition conditions for 48 hours). Mass spectrometric analysis consistently identified desmosome junction components, particularly Desmoplakin (DSP) and Vimentin (VIM), as binding partners of HER2 across LD and HD conditions (Figure 3F and S3B-C). Co-immunoprecipitation experiments in MCF10A-Teti-HER2_GFP cells treated with 1 µM Dox under medium density (10,000 cells/cm^2) conditions for 72 hours confirmed the physical interaction of HER2 with DSP and VIM proteins (Figure 3G). Notably, no binding was observed for α and β Catenin proteins, which share a role similar to DSP in the formation of primary junctions in epithelial cells (Figure S3D). Interestingly, we found that mRNA expression level of desmosome junctions, rather than tight or adherent junctions, were upregulated in MCF10A-Teti-HER2_GFP cells treated with 1 µM Dox after 3 days of culture under LD conditions. Our qPCR expression analyses revealed that desmosome junctions represented more stable cell junctions compared to tight and adherent junctions, although they gradually lost their expression profile during long-term culture (15 days) (Figure S3E).

Subsequently, we aimed to simulate the route of cancer cell dissemination by creating a mixed culture environment that included MCF10A-Teti-HER2_GFP cells along with various cell types and extracellular matrix (ECM) conditions. Our objective was to explore the potential of cell contacts in inducing HER2 membrane localization in MCF10A-Teti-HER2_GFP cells. Intriguingly, our findings demonstrated that certain epithelial cell lines possessed the ability to facilitate HER2 localization to the cell membrane of MCF10A-Teti-HER2_GFP cells after 24 hours of co-culture, while others lacked this capability (Figure 3H and I). Notably, mRNA expression analyses of these cells indicated higher expression levels of desmosome junction surface cadherin molecules (DSC1-3 and DSG1-3) in cells that had a greater capacity to facilitate HER2 localization to the membrane compared to those lacking this ability (Figure 3J). It seems that increased desmosome cadherin protein expression increases stickiness of cancer cells to initiate cell contact.

To deepen our understanding of the role of desmosome junctions and DSP in regulating HER2 membrane localization and initiating proliferation, we executed a DSP siRNA knockdown in MCF10A-Teti-HER2_GFP cells and cultured them under both low and high cellular densities. While DSP knockdown had no evident impact on cell proliferation in HD (Figure S3F), it markedly diminished cell-

cell contact and proliferation in LD conditions (Figure 3K). Furthermore, the intensity of HER2 and DSG2 decreased at the cell contact surfaces of contacting cells upon DSP knockdown (Figure 3L).

In summary, our results strongly suggest the involvement of desmosome junctions, particularly DSP, in regulating HER2 membrane localization and initiating proliferation. This mechanism holds significant implications for our understanding of cancer cell colonization at distant sites.

Changing on the function of endoplasmic reticulum (ER) accumulates HER2 inside of the cells in low density:

As HER2 expression levels were found to be higher in the nuclear fraction of LD compared to HD MCF10A-Teti-HER2_GFP (1 µM Dox) and MCF7 cells (Figure S1D and 2C), we aimed to investigate the precise cellular localization of HER2 when it is not present in the membrane. To achieve this, we conducted confocal imaging, which revealed that HER2 was located not within the nucleus but in close proximity to the nucleus (Figure 4A). Notably, the nuclear envelope, comprised of a double membrane bilayer originating from the endoplasmic reticulum (ER) membrane, forms the most obvious boundary around the nucleus. Hence, we cultured MCF10A-Teti-HER2_GFP cells at both low (2000 cells/cm^2) and high (20000 cells/cm^2) cellular densities for 72 hours and stained them with an ER tracking dye marker. The results demonstrated a strong correlation between HER2 and the ER in LD, but not in HD (Figure 4B-C). Furthermore, we developed a cell organelle fractionation protocol (see methods) and showed that the nuclear/cytoplasmic accumulation of HER2 (NER) correlates with the fraction enriched in calnexin (CLNX) protein, a typical marker for the ER organelle (Figure S4A).

Previous studies have established that ER membranes are physiologically active, interacting with the cytoskeleton and containing specialized domains for distinct functions. Among these functions, two critical roles of the ER are regulating calcium ion gradients for cell migration (*27*) and participating in protein trafficking (*28*). To investigate the role of the ER in HER2 localization concerning protein trafficking, we treated MCF10A-Teti-HER2_GFP (1 µM Dox) and MCF7 cells at moderate density (2500 cells/cm^2 for MCF7 and 10000 cells/cm^2 for MCF10A-Teti-HER2_GFP) with Brefeldin A (BFA; 50 µg/ml) for 24 hours, an agent inhibiting protein trafficking from the ER to the Golgi apparatus. We observed that BFA-treated cells exhibited increased non-membrane (correlation to NER) HER2 levels, and a higher number of single cells compared to the control (Figure 4D and S4B). Due to its strong toxicity impact on cells, we excluded proliferation and migration functional experiments for the BFA treatments. Furthermore, we examined the involvement of RAB1A (a small GTPase regulating vesicle traffic from the ER to the Golgi apparatus) and SEC24A (a component of COPII-coated vesicles mediating protein transport from the ER) (Figure S4C). The protein expression levels of both markers increased upon HER2 activation. Moreover, RAB1A expression was upregulated in HD compared to LD, indicating a decrease in protein trafficking function in the ER due to reduced cell density (Figure S4D).

Another important role of the ER, particularly in cell migration, is providing calcium ions at the leading edge of the cell, essential for cell movement (*27*). This function is tightly regulated by the phospholipase C (PLC) protein (*29*). To investigate the role of the ER and PLC in regulating HER2 cellular localization, we seeded MCF10A-Teti-HER2_GFP (1 µM Dox) and MCF7 cells at LD (500 cells/cm^2 for MCF7 and 2000 cells/cm^2 for MCF10A-Teti-HER2_GFP) and treated them with 1 µM of a PLC inhibitor for 6 hours followed by a 24-hour incubation. We observed that pharmacological inhibition of PLC caused an increase in HER2 membrane localization, resulting in increased cell proliferation and

decreased cell motility (Figure 4E and S4E). Furthermore, the protein expression levels of PLC and p-PLC decreased in MCF10A-Teti-HER2_GFP HD cells (Figure S4F). Additionally, we indirectly disrupted PLC function by treating MCF10A-Teti-HER2_GFP and MCF7 cells (2000 cells/cm^2 for MCF7 and 10000 cells/cm^2 for MCF10A-Teti-HER2_GFP) with 0.5 mM of EGTA, a calcium ion chelating agent. After 24 hours of treatment, HER2 was released from perinuclear structures (Figure S4G). Due to its strong toxicity impact on cells, we excluded proliferation and migration functional experiments for the ETGA treatments. Moreover, we analyzed the arrangement of cell organelles within MCF7 cells as single migratory cells compared to cells in compact structures using transmission electron microscopy. We found that the soft-ER, responsible for providing calcium ions at the leading edge of migratory cells (*30*) was polarized towards the leading membrane edge of cells compared to cells within compact structures in HD (Figure 4F).

In conclusion, we have determined that the function of the ER shifts between protein trafficking and calcium ion flux depending on cell density. Under LD conditions, the protein trafficking function of the ER is diminished, leading to HER2 accumulation in ER structures. The primary function of the ER in LD is the regulation of calcium through the PLC pathway at the leading edge of migrating cells.

Competition between PLC and PDPK1 regulates switches between migration or proliferation phenotype:

Once HER2 is positioned on the cell membrane and stabilized, it can activate the PI3K pathway. Subsequently, PI3K converts PIP2 to PIP3. PIP3 can then bind to proteins containing PH domains, triggering proliferation (*31*). On the other hand, some of the PH domain proteins in the HER2-PI3K pathway have a certain degree of affinity for PIP2 (*31, 32*), which is the primary substrate targeted by the PLC pathway (*31*). In the low-density condition, we observed the activation and significance of the PLC pathway. Consequently, we postulated that there might be competition for PIP2 binding/usage between PLC and PI3K pathways. Specifically, in this scenario, the PI3K pathway utilizes PIP2 and converts it into PIP3. Furthermore, under high-density (HD) or high-HER2-expression conditions, there is an upregulation of PH domain proteins within the PI3K pathway. This upregulation may lead to an increased occupancy of PIP2 molecules, potentially resulting in the inactivation of the PLC pathway. Consequently, this competitive relationship between the two pathways could serve as a fundamental molecular switch that influences the balance between cellular proliferation and migration.

To test this hypothesis, we conducted immunostaining for PIP2 and PIP3 in MCF10A-Teti-HER2_GFP cells treated with 1uM Dox. The results revealed a depletion of PIP2 at the cell-cell contact surface where HER2 localizes to the membrane (Figure 5A-B). PIP3 staining exhibited partial overlap with HER2 staining, although the results were not as distinct as the PIP2 staining (Figure S5A).

To determine if PH domain proteins are upregulated or co-regulated with HER2 expression, we assessed the protein expression of PDPK1, AKT1, AKT2, AKT3, and SIN1 in MCF10A-Teti-HER2_GFP cells treated with Dox. We observed an upregulation/co-regulation of protein expression for AKT1, AKT3, SIN1, and PDPK1 along with HER2 expression (Figure 5C).

Subsequently, we performed a Protein-Lipid Overlay assay (PLO), in which we incubated PH domain peptides of candidate proteins with fixed PIP2 spots on immunoblotting papers. Our results indicated that both Sin1 and PDPK1 can bind to PIP2, with PDPK1 showing a concentration-dependent gradient of binding (Figure 5D-E). Furthermore, our qPCR analyses showed that only PDPK1 among all

PH domain candidates was upregulated by HER2 levels, displaying a HER2-dose-dependent expression pattern (Figure S5B-C). Additionally, we demonstrated that the protein expression of PLC and p-PLC decreased upon HER2 upregulation or an increase in the cell density (Figure 5C and S4F). Based on these findings, we concluded that PIP2 is a shared substrate for both proliferation and migration pathways, and PDPK1 could potentially be the key regulator in the switch from proliferation to migration in high-HER2 expressing cells and high-density condition.

We then determined the optimal concentration of GSK 2334470 (a pharmacological inhibitor of PDPK1) that inhibited proliferation while keeping the cells alive (relative quantification compared to the starved medium control) (Figure S5E). Subsequently, SKBR3 cells were treated with 1uM GSK 2334470 for 48 hours and then reseeded in low-density conditions under 1uM GSK 2334470 treatment, followed by an additional two-day incubation. We observed that PDPK1 inhibition could rescue perinuclear (NER) HER2 localization in SKBR3 as a high-HER2 expressing cells, which had not been observed previously (Figure 5F).

Subsequently, we proceeded to overexpress the PH domain of PDPK1, referred to as PH-PDPK1, in both the MCF10A-Teti-HER2_GFP and MCF7 cell lines (Figure S5F). Intriguingly, the overexpression of PH-PDPK1 protein led to a significant reduction in the cellular localization of HER2 in both MCF7 and MCF10A-Teti-HER2_GFP cells under LD conditions. Notably, this overexpression of PH-PDPK1 resulted in promoting higher proliferation and reduced motility of cells (Figure 5G-J and S5G-I). However, it is worth noting that PH-PDPK1 overexpression did not elicit changes in the motility ability of MCF7 cells. This difference may be attributed to the smaller impact on the proliferation of MCF7 cells compared to MCF10A-Teti-HER2_GFP cells and the distinct motility characteristics of the two cell types (Figure S5J). These results confirm the role of PDPK1 on the regulation of molecular switch at the membrane level.

Altogether, these results, along with the membrane HER2 localization results, elucidated the molecular switch mechanism from migration to proliferation and how cell-cell junctions and the activation of HER2 can concurrently regulate the migration of cancer cells (Figure 5K).

Patient sample analyses confirms various aspects of plasticity mechanism found *in vitro*:

To investigate clinical relevance of our mechanistic findings, we conducted an analysis of the cellular positioning of HER2 in circulating tumor cells (CTCs) and clusters that had been identified using the Cellsearch system, based on Cytokeratin (CK5, 7, 8,18,19) and HER2 staining. We examined 429 cells and clusters obtained from M1 breast cancer patients with HER2+ status in their primary tumors (Figure S6A-C).

For single-cell analyses, we identified three distinct patterns of HER2 staining. Approximately half of the single cells exhibited spotty staining, which rationally cannot be considered as classical membrane HER2 staining. Our criteria for membrane staining required at least 50% membrane staining. Therefore, we focused our analyses on the remaining cells without the spotty staining pattern. Interestingly, we discovered that the majority of single CTCs with a non-spotty pattern exhibited cytoplasmic/non-membrane HER2 staining (38.75% non-membrane vs. 17.8% membrane staining). Remarkably, when analyzing cluster circulating cells, we observed that most of the clusters (89% membrane staining vs. 11% non-membrane staining) displayed a membrane staining pattern. More intriguingly, all the HER2 membrane staining was concentrated in the cell-cell contact surfaces (Figure 6 A and S6A), mirroring what we observed in our *in vitro* results (Figure 3A-C).

Further, we analyzed 14 primary tumor and metastasis samples from six M1 breast cancer patients with HER2-positive status in their primary tumors. We used imaging mass cytometry techniques to evaluate proliferation, migration, stemness, and desmosome junctions in solitary cancer cells separated from their epithelial compartments as compared to cluster compact epithelial structures. A pan cytokeratin staining (CK5, 7, 8,18,19) was employed as a detector of cancer cells, and a panel of antibodies was used to track our target phenotypes, including HER2 as the main candidate to track its cellular localization, KI67 as a proliferation marker, CDH1 (Ecad), VIM, and ZEB1 as EMT and migration markers, JUP (plakoglobin) as a desmosome junction marker, and ALDH1 as a stemness marker in HER2 breast cancer subtype.

Our results indicated that 88% of solitary HER2-positive cells exhibited non-membrane/cytoplasmic staining for HER2, which is nearly double the percentage of cytoplasmic staining (45%) in the cluster cells (Figure 6B and C). Interestingly, the number of KI67-positive cells was much lower in solitary single cells than in cluster cells. Conversely, the number of ZEB1-positive cells was significantly higher in solitary single cells compared to the cells in cluster structures (Figure 6D and E). Moreover, the intensity of the signal and percentages of high expressing cell lines for ALDH1 and plakoglobin was significantly higher in single cells compared to the clusters (Figure S6D and E).

Remarkably, when we assessed the correlation between HER2 cellular positioning and KI67 and ZEB1 positivity, we found that solitary single cells with membrane HER2 staining were significantly less KI67-positive than cluster cells with membrane HER2 staining. Conversely, cytoplasmic HER2 staining solitary cells were more ZEB1-positive compared to cytoplasmic HER2 staining cluster cells (Figure 6F). These findings may indicate the transition state of solitary cells from a proliferative phenotype to a migratory/mesenchymal state as they lose their cell contacts.

In summary, our study reveals a clinical manifestation of the plasticity mechanism we uncovered. Loss of cell contact upon dissemination prompts a shift in HER2 cellular localization, reflecting a transition from proliferation to migration, as observed in patient samples. These findings underscore the clinical relevance of our mechanistic insights into cancer cell behavior, shedding light on the phenotypic changes that occur during metastasis.

Discussion:

Our study presents significant findings that reshape our understanding of cancer cell plasticity in HER2-positive breast cancer. These findings introduce novel insights into HER2 subcellular localization, endoplasmic reticulum (ER) function, and the role of desmosome junctions in the regulation of cancer cell phenotypic switching between migration and proliferation.

Our research distinctly elucidates the subcellular localization of HER2. Specifically, we have demonstrated that, when HER2 is not membrane-bound, it accumulates within perinuclear ER organelles. This definitive clarification settles previous debates concerning the intracellular positioning of ERBB family proteins(*33-39*).

We also reveal a profound shift in ER function, transitioning from its established role in protein trafficking to a regulator of calcium flux via the PLC pathway. This transition in ER function is a critical determinant in modulating the HER2 oncogenic pathway, thereby influencing cancer cell phenotypic switching.

An essential aspect of our research focuses on the discovery of a molecular switch mechanism. We identify the pivotal role of desmosome junctions in facilitating early cell-cell contacts among cancer cells. In situations of cell junction loss or low cell density, an epithelial-to-mesenchymal transition (EMT) program is activated in epithelial cells, resulting in a significant upregulation of desmosome junctions. Remarkably, desmosome junctions endure as the last remaining epithelial cell contacts for disseminated cancer cells, exhibiting prolonged upregulation compared to other epithelial junctions. Furthermore, we establish a connection between the expression of cadherin genes (DSC1-3 and DSG1-3) and what we term "stickiness" in cancer cells. Our discovery of a physical binding between HER2 and DSP, serving as the core of desmosome junction assembly (*40*), highlights that elevated expression of these adhesive proteins enhances cancer cells' propensity to form junctions. This, in turn, facilitates HER2 localization and promotes proliferation. Our results provide mechanistic insights that elucidate recent findings in studies where DSC2 or plakoglobin expression in breast cancer cells conferred resistance to fluid shear stress and increased their ability to form clusters post-dissemination (*41-43*). Intriguingly, our Imaging Mass Cytometry (IMC) results corroborate this notion, illustrating a phenotypic switch in solitary single cancer cells with elevated plakoglobin, increased ZEB1, and reduced KI67 protein levels.

Another novel aspect of our study concerns the molecular switch occurring on the cell membrane when new cell contacts are established through desmosome junctions. Upon HER2 localization to the membrane, a competition arises between the HER2 pathway and the PLC pathway for the occupation/using of PIP2 molecules. HER2 activation triggers the PI3K pathway, converting PIP2 to PIP3. Simultaneously, HER2 activation upregulates PDPK1, which features a PH domain with a high binding affinity to PIP2. Consequently, HER2 activation consumes and occupies all available PIP2 molecules, inhibiting PLC pathway activity and steering cells towards a proliferative state. This mechanistic revelation elucidates previous observations that overactivation of the HER2 pathway can transition cells from a migratory phenotype to a proliferative one (*14*).

Contrary to previous studies focusing on nuclear ERBB function, particularly interactions with STAT proteins and the JAK-STAT signaling pathway(*44-46*), our research presents findings that do not align with such localization. Nevertheless, a comprehensive analysis is warranted to fully comprehend the role of perinuclear HER2.

In summary, our study introduces a pioneering cancer cell plasticity mechanism governing the phenotypic switch between proliferation and migration in HER2-positive breast cancer. This mechanism assumes a pivotal role in the dissemination and colonization of cancer cells. Most notably, our findings offer fresh prospects for targeted therapies designed to eliminate cancer cells during their latent phase, prior to colonization.

Methods and materials: See supplementary Methods and materials.

Acknowledgements: This work was supported by grants from the DFG (HO 6175/4-1, SFB TRR305-A05 and Deutsche Krebshilfe (70114988).

References:

1. A. Dasgupta, A. R. Lim, C. M. Ghajar, Circulating and disseminated tumor cells: harbingers or initiators of metastasis? *Molecular oncology* **11**, 40-61 (2017).

2. C. A. Klein, Parallel progression of primary tumours and metastases. *Nature reviews. Cancer* **9**, 302-312 (2009).
3. H. Hosseini *et al.*, Early dissemination seeds metastasis in breast cancer. *Nature*, (2016).
4. K. L. Harper *et al.*, Mechanism of early dissemination and metastasis in HER2(+) mammary cancer. *Nature*, (2016).
5. C. L. Chaffer, B. P. San Juan, E. Lim, R. A. Weinberg, EMT, cell plasticity and metastasis. *Cancer metastasis reviews* **35**, 645-654 (2016).
6. H. Jayatilaka *et al.*, Tumor cell density regulates matrix metalloproteinases for enhanced migration. *Oncotarget* **9**, 32556-32569 (2018).
7. G. M. Sharif *et al.*, Cell growth density modulates cancer cell vascular invasion via Hippo pathway activity and CXCR2 signaling. *Oncogene* **34**, 5879-5889 (2015).
8. Y. Fan, T. Meyer, Molecular control of cell density-mediated exit to quiescence. *Cell reports* **36**, 109436 (2021).
9. J. W. O'Connor, K. Mistry, D. Detweiler, C. Wang, E. W. Gomez, Cell-cell contact and matrix adhesion promote αSMA expression during TGFβ1-induced epithelial-myofibroblast transition via Notch and MRTF-A. *Sci Rep* **6**, 26226 (2016).
10. Y.-H. Chen *et al.*, Loss of cell–cell adhesion triggers cell migration through Rac1-dependent ROS generation. *Life Science Alliance* **6**, e202201529 (2023).
11. M. A. Cichon, C. M. Nelson, D. C. Radisky, Regulation of epithelial-mesenchymal transition in breast cancer cells by cell contact and adhesion. *Cancer informatics* **14**, 1-13 (2015).
12. J. Ursini-Siegel, B. Schade, R. D. Cardiff, W. J. Muller, Insights from transgenic mouse models of ERBB2-induced breast cancer. *Nature reviews. Cancer* **7**, 389-397 (2007).
13. H. Liu *et al.*, MYC suppresses cancer metastasis by direct transcriptional silencing of alphav and beta3 integrin subunits. *Nature cell biology* **14**, 567-574 (2012).
14. J. N. Hutchinson, J. Jin, R. D. Cardiff, J. R. Woodgett, W. J. Muller, Activation of Akt-1 (PKB-alpha) can accelerate ErbB-2-mediated mammary tumorigenesis but suppresses tumor invasion. *Cancer research* **64**, 3171-3178 (2004).
15. O. J. Sansom *et al.*, Loss of Apc allows phenotypic manifestation of the transforming properties of an endogenous K-ras oncogene *in vivo*. *Proc Natl Acad Sci U S A* **103**, 14122-14127 (2006).
16. A. Q. Kohrman, D. Q. Matus, Divide or Conquer: Cell Cycle Regulation of Invasive Behavior. *Trends in cell biology* **27**, 12-25 (2017).
17. A. Patel, N. Unni, Y. Peng, The Changing Paradigm for the Treatment of HER2-Positive Breast Cancer. *Cancers* **12**, (2020).
18. D. E. Carvajal-Hausdorf *et al.*, Measurement of Domain-Specific HER2 (ERBB2) Expression May Classify Benefit From Trastuzumab in Breast Cancer. *Journal of the National Cancer Institute* **107**, (2015).
19. D. Grassini *et al.*, Unusual Patterns of HER2 Expression in Breast Cancer: Insights and Perspectives. *Pathobiology : journal of immunopathology, molecular and cellular biology* **89**, 278-296 (2022).
20. H. S. Won *et al.*, Clinical significance of HER2-low expression in early breast cancer: a nationwide study from the Korean Breast Cancer Society. *Breast Cancer Research* **24**, 22 (2022).
21. D. Y. Oh *et al.*, HER2 as a novel therapeutic target for cervical cancer. *Oncotarget* **6**, 36219-36230 (2015).
22. L. F. Abrahao-Machado, C. Scapulatempo-Neto, HER2 testing in gastric cancer: An update. *World journal of gastroenterology* **22**, 4619-4625 (2016).
23. M. J. M. Magbanua *et al.*, Genomic and expression profiling reveal molecular heterogeneity of disseminated tumor cells in bone marrow of early breast cancer. *npj Breast Cancer* **4**, 31 (2018).
24. C. Lopes *et al.*, HER2 Expression in Circulating Tumour Cells Isolated from Metastatic Breast Cancer Patients Using a Size-Based Microfluidic Device. *Cancers* **13**, (2021).

25. B. Rack *et al.*, Comparison of HER2 Expression in Primary Tumor and Disseminated Tumor Cells in the Bone Marrow of Breast Cancer Patients. *Oncology* **90**, 232-238 (2016).
26. B. A. S. Jaeger *et al.*, The HER2 phenotype of circulating tumor cells in HER2-positive early breast cancer: A translational research project of a prospective randomized phase III trial. *PloS one* **12**, e0173593 (2017).
27. F. C. Tsai, G. H. Kuo, S. W. Chang, P. J. Tsai, Ca2+ signaling in cytoskeletal reorganization, cell migration, and cancer metastasis. *BioMed research international* **2015**, 409245 (2015).
28. E. M. Wenzel, L. A. Elfmark, H. Stenmark, C. Raiborg, ER as master regulator of membrane trafficking and organelle function. *The Journal of cell biology* **221**, (2022).
29. A. S. Hammad, K. Machaca, Store Operated Calcium Entry in Cell Migration and Cancer Metastasis. *Cells* **10**, (2021).
30. K. Hayashi, T. S. Yamamoto, N. Ueno, Intracellular calcium signal at the leading edge regulates mesodermal sheet migration during Xenopus gastrulation. *Scientific Reports* **8**, 2433 (2018).
31. W. S. Park *et al.*, Comprehensive identification of PIP3-regulated PH domains from C. elegans to H. sapiens by model prediction and live imaging. *Molecular cell* **30**, 381-392 (2008).
32. M. P. Scheid, M. Parsons, J. R. Woodgett, Phosphoinositide-dependent phosphorylation of PDK1 regulates nuclear translocation. *Molecular and cellular biology* **25**, 2347-2363 (2005).
33. L. K. Johnson, I. Vlodavsky, J. D. Baxter, D. Gospodarowicz, Nuclear accumulation of epidermal growth factor in cultured rat pituitary cells. *Nature* **287**, 340-343 (1980).
34. C. Y. Ni, M. P. Murphy, T. E. Golde, G. Carpenter, gamma -Secretase cleavage and nuclear localization of ErbB-4 receptor tyrosine kinase. *Science (New York, N.Y.)* **294**, 2179-2181 (2001).
35. M. Offterdinger, C. Schöfer, K. Weipoltshammer, T. W. Grunt, c-erbB-3: a nuclear protein in mammary epithelial cells. *The Journal of cell biology* **157**, 929-939 (2002).
36. S. C. Wang *et al.*, Binding at and transactivation of the COX-2 promoter by nuclear tyrosine kinase receptor ErbB-2. *Cancer cell* **6**, 251-261 (2004).
37. K. Dittmann *et al.*, Radiation-induced epidermal growth factor receptor nuclear import is linked to activation of DNA-dependent protein kinase. *The Journal of biological chemistry* **280**, 31182-31189 (2005).
38. F. D. Cuello-Carrión *et al.*, HER2 and β-catenin protein location: importance in the prognosis of breast cancer patients and their correlation when breast cancer cells suffer stressful situations. *Clinical & experimental metastasis* **32**, 151-168 (2015).
39. L. Ma *et al.*, JWA down-regulates HER2 expression via c-Cbl and induces lapatinib resistance in human gastric cancer cells. *Oncotarget; Vol 7, No 44*, (2016).
40. O. Nekrasova, K. J. Green, Desmosome assembly and dynamics. *Trends in cell biology* **23**, 537-546 (2013).
41. K. Li, R. Wu, M. Zhou, H. Tong, K. Q. Luo, Desmosomal proteins of DSC2 and PKP1 promote cancer cells survival and metastasis by increasing cluster formation in circulatory system. *Science Advances* **7**, eabg7265 (2021).
42. F. Reimer *et al.*, The role of the desmosomal protein desmocollin 2 in tumour progression in triple negative breast cancer patients. *Cancer Cell International* **23**, 47 (2023).
43. N. Aceto *et al.*, Circulating Tumor Cell Clusters Are Oligoclonal Precursors of Breast Cancer Metastasis. *Cell* **158**, 1110-1122 (2014).
44. R. I. Cordo Russo *et al.*, Targeting ErbB-2 nuclear localization and function inhibits breast cancer growth and overcomes trastuzumab resistance. *Oncogene* **34**, 3413-3428 (2015).
45. R. I. Cordo Russo, M. F. Chervo, S. Madera, E. H. Charreau, P. V. Elizalde, Nuclear ErbB-2: a Novel Therapeutic Target in ErbB-2-Positive Breast Cancer? *Hormones & cancer* **10**, 64-70 (2019).
46. C. C. Williams *et al.*, The ERBB4/HER4 receptor tyrosine kinase regulates gene expression by functioning as a STAT5A nuclear chaperone. *The Journal of cell biology* **167**, (2004).

Main Figures

Figure 1:

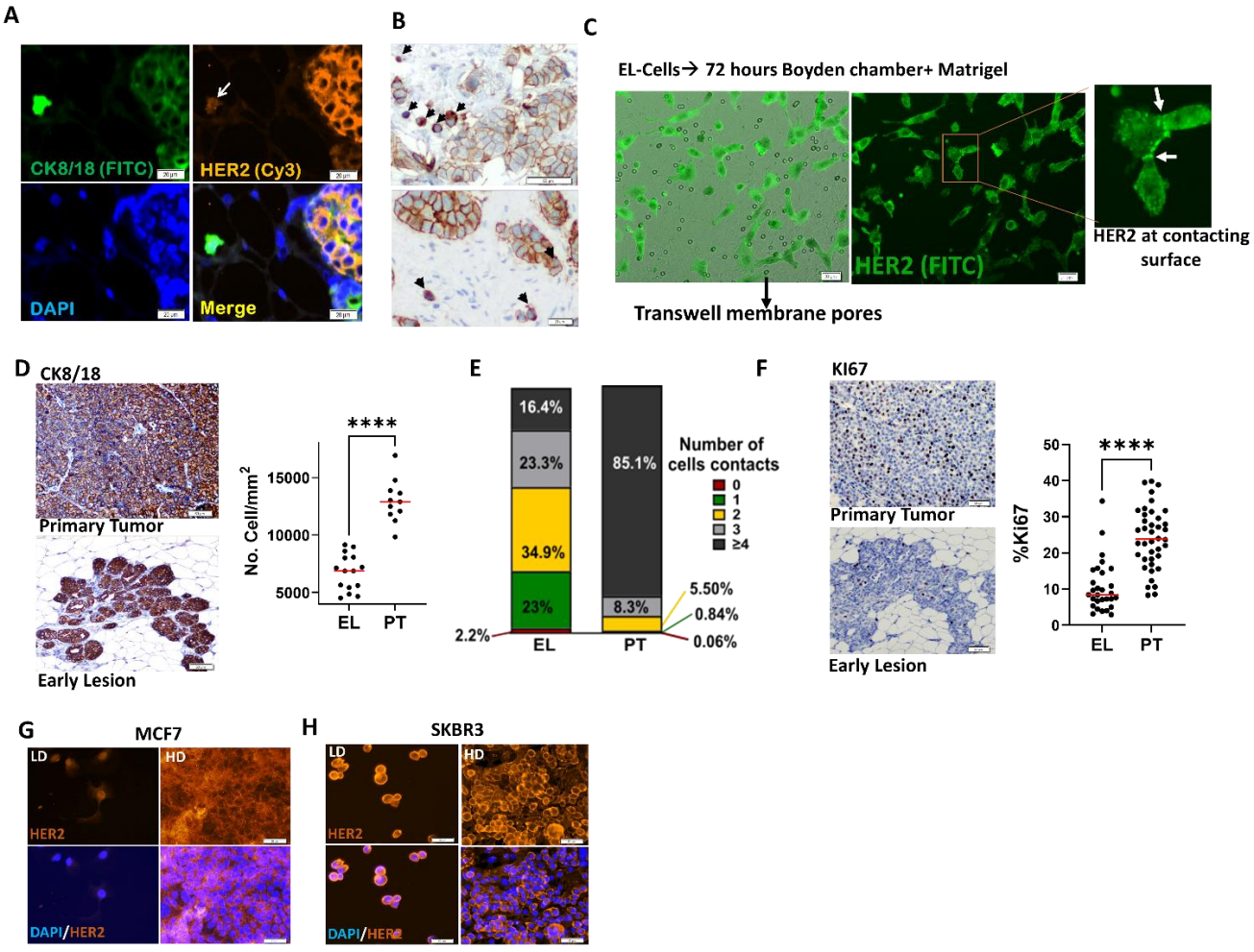

Figure 1: Cell-cell contact, cellular density, and HER2 expression levels are intricately linked to the membrane localization of HER2 and the phenotypic switch in breast cancer cells. A) Non-membrane HER2 localization in solitary cancer cells within primary lesions from the BALB-neuT mouse model. HER2 is labeled with Cy3, and CK8/18 with FITC. **B**) HER2 staining in HER2+ human breast primary tumor (PT) samples with HER2 IHC scores +1, +2, and +3, highlighting solitary cancer cells (indicated by arrows) exhibiting distinct HER2 cellular localization compared to cells within the tumor mass. **C**) *In vitro* invasion assay for cancer cells isolated from EL lesions of BALB-NeuT, revealing migrating cells on the opposite side of the Boyden chamber's membrane, lacking HER2 staining on the cell membrane (as seen in the FITC channel), with HER2 exclusively localized at the cell-cell contact surface (indicated by arrows). Boyden chambers were coated with 40% Matrigel, and 50,000 cells per 24-well insert were cultured for 72 hours, with FCS-free medium above and FCS-containing medium below the chamber. **D**) Confirmation of tight epithelial structures in PT compared to EL lesions in BALB-neuT samples through cytokeratin (CK8/18) staining. **E**) Quantification showing reduced cell contacts in cells within EL structures compared to those within PT structures of BALB-NeuT, presented as a percentage graph obtained by counting cell contacts from five CK8/18 staining images per case. **F**) Increased frequency of Ki67+ cells in PT tight structures compared to EL in BALB-neuT samples, indicating higher proliferation levels. **G-H**) Cellular localization of HER2 in low and high-HER2 expressing cell lines at varying cell culture densities. In cell lines with low to moderate HER2 expression, such as MCF7 (G), HER2 localizes to the cytoplasmic-nuclear compartment at low cell density (500 cells/cm2; 72-hour culture) but shifts to membrane localization at high cell density (20,000 cells/cm2; 72-hour culture). Conversely, in SKBR3 cells, a HER2+ cell line with strong HER2 expression, HER2 remains consistently

localized to the membrane regardless of cell density. See also Extended Data Fig. S1C and S1E-G. All p-values calculated using Student t-test; data in panels D and F are presented as means.

Figure 2:

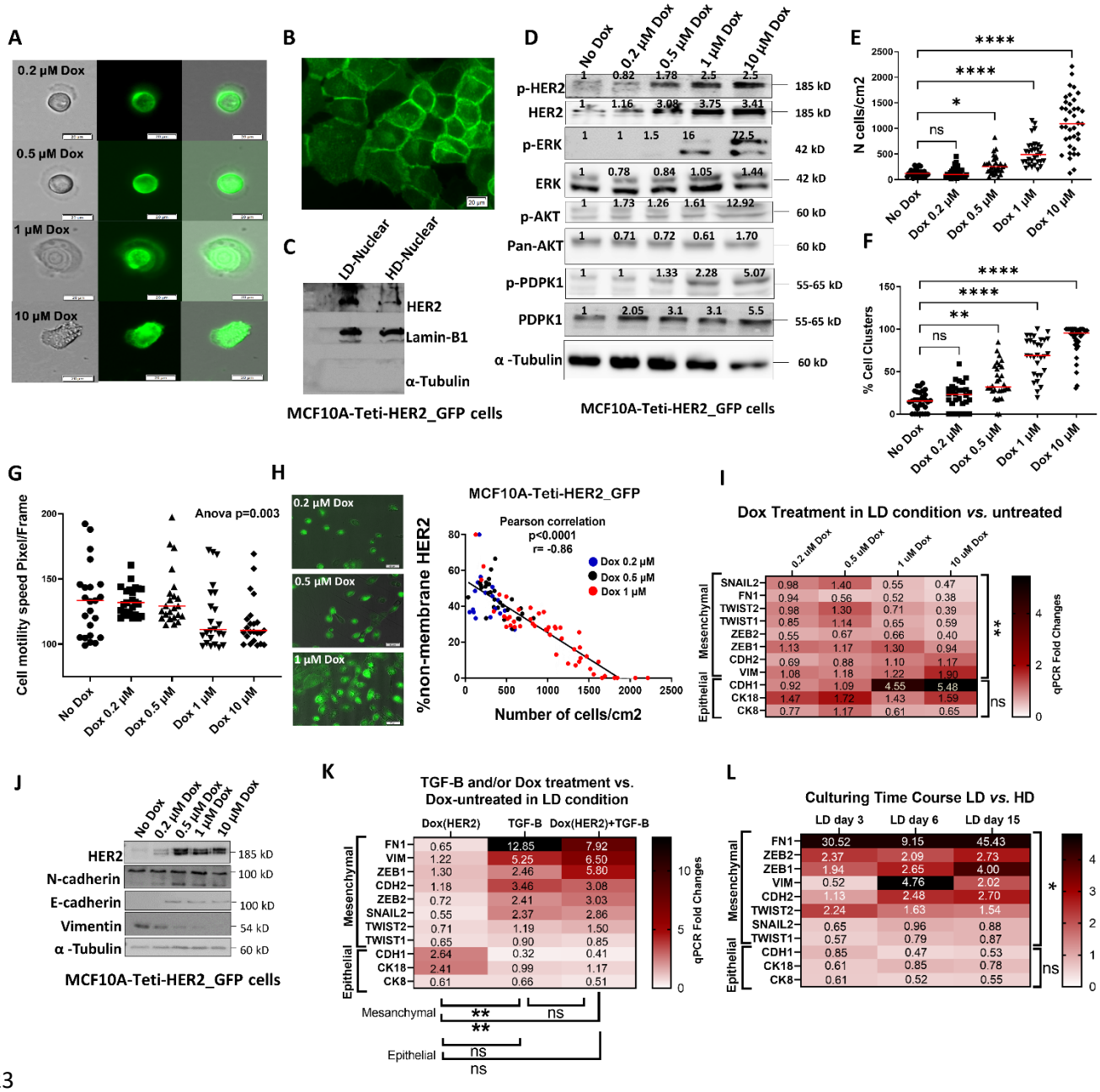

Figure 2: ***In vitro*** **modeling of HER2 expression levels and cell density regulation of HER2 cellular localization and phenotypic cell transitions. A-B**) HER2 cellular localization in low density (LD) and high density (HD) conditions in MCF10-Teti-HER2_GFP cells. Low to moderate expression of HER2 (Dox 100nM to 1 µM) resulted in similar LD images with non-membrane HER2_GFP, whereas high expression of HER2 (Dox 10 µM) led to membrane bound HER2 (A). In HD conditions, HER2 was consistently located on the cell membrane regardless of HER2 expression levels (B). **C**) Immunoblotting for the nuclear fraction of MCF10A-Teti-HER2_GFP cells in LD and HD. Lamin B1 served as the loading control for the nuclear fraction, and α-Tubulin as the loading control for the cytoplasmic fraction. The absence of Tubulin in the nuclear fraction indicates the absence of cytoplasmic contamination in the nuclear fraction. **D**) Protein expression levels of p-ERK, p-PDPK1, and p-AKT increase upon HER2 activation, confirming that HER2 expression can enhance cell proliferation. **E-F**) Inducing HER2 expression levels increases cell proliferation, leading to higher cell density (E) and the formation of more cell clusters (F). **G**)

Increasing HER2 expression levels reduces the migration ability of MCF10A-Teti-HER2_GFP cells, as indicated by cell motility per frame. Cells were cultured in low density (LD) conditions (2000 cells/cm2) for 24 hours before image acquisition, and cell monitoring and image acquisition were conducted every 10 minutes over 24 hours. **H**) Induction of HER2 expression levels enhances cell proliferation, subsequently leading to higher cell density and a reduction in non-membrane HER2. Cells were cultured for 72 hours in LD conditions (2000 cells/cm2) and treated with varying concentrations of Dox. The X-axis represents the final cell counts at the time of image acquisition. **I**) qPCR results depict the expression levels of epithelial-mesenchymal transition (EMT) markers in MCF10A-Teti-HER2_GFP cells cultured for 72 hours in LD conditions (2000 cells/cm2) and treated with different Dox concentrations (0.2-1 µM) compared to untreated cells. **J**) Immunoblotting results of MCF10A-Teti-HER2_GFP cells cultured for 72 hours in LD conditions (2000 cells/cm2) and treated with various Dox concentrations, demonstrating that HER2 expression also modulates EMT markers at the protein level. Increasing HER2 expression induces E-cadherin expression and reduces Vimentin protein levels. **K**) qPCR results of EMT markers in MCF10A-Teti-HER2_GFP cells cultured for 72 hours in LD conditions (2000 cells/cm2) and treated with TGF-B (5 ng/ml daily) with or without Dox (1 µM). Notably, HER2 expression alone could not reverse the mesenchymal phenotype. **L**) Prolonged culturing of cells in LD conditions intensifies the induction of the mesenchymal state in MCF10A-Teti-HER2_GFP cells. P-values in panels G and I were calculated using a two-way ANOVA test. P-values in panel L were calculated using student paired t-test between days 3 and 15. P-values in panels E and F were calculated using the Mann-Whitney U test. The p-value in panel H is presented from the Pearson correlation test. Data in panels E, F, and G are represented as medians.

675 # Figure 3:

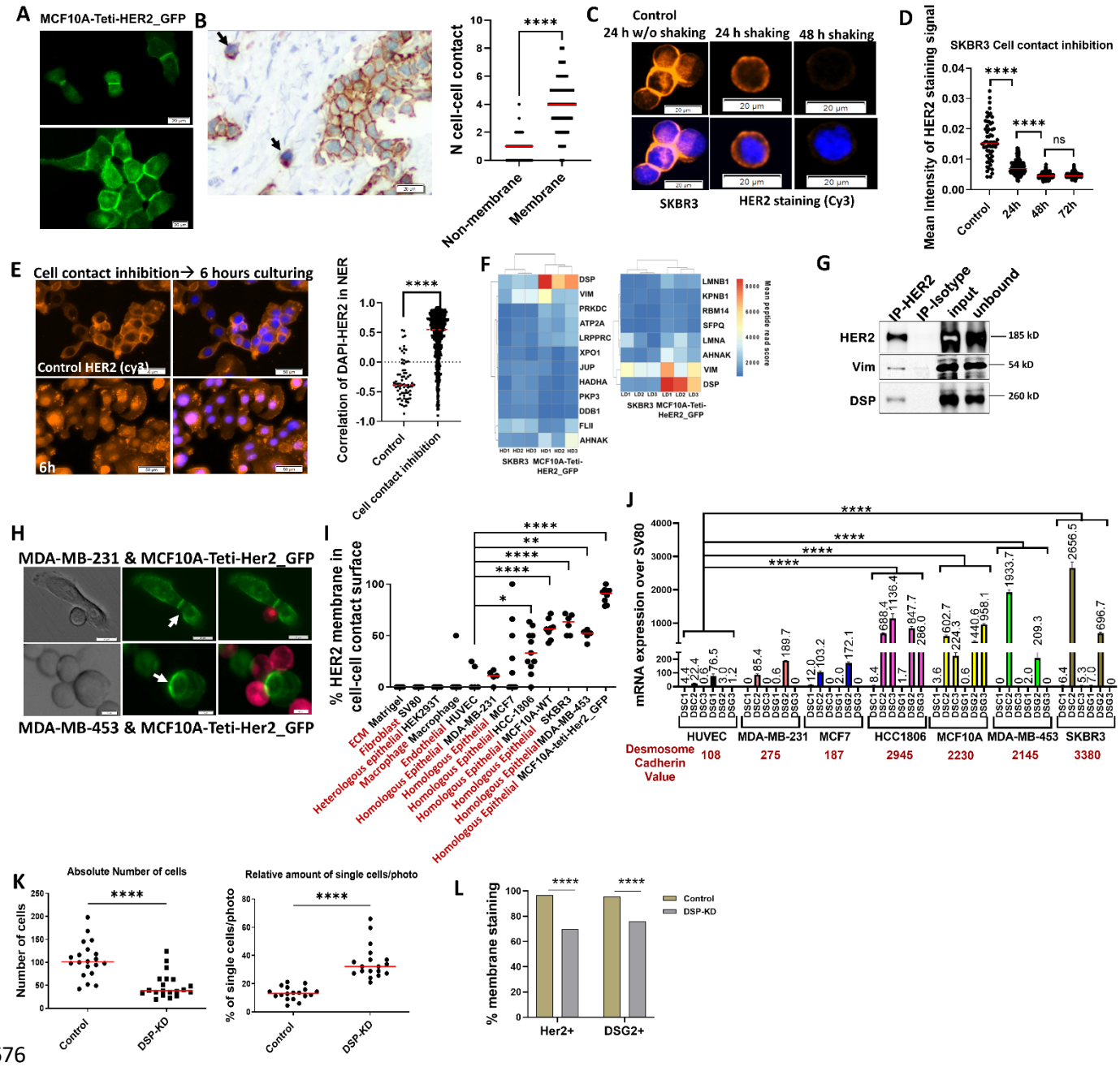

676

677 **Figure 3: Desmosome Junctions Initiate HER2 Membrane Localization in Early Cell-Cell Contacts. A**) Cell-cell
678 contact is essential for HER2 membrane localization and stabilization. HER2 is expressed on the cell membrane
679 when two cells make contact. **B**) HER2 staining in a primary breast tumor (HER2 IHC scores 1+, 2+, 3+). Arrows
680 indicate solitary cancer cells separated from the tumor mass structure with different HER2 cellular localization
681 compared to the cells in the tumor mass. The right graph quantifies HER2 non-membrane localization and the
682 number of cell contacts. An increase in the number of cell-cell contacts (an indicator of cell density) leads to
683 increased membrane HER2 localization. **C**) SKBR3 cells cultured in non-adherent conditions and shaken for 48
684 hours to inhibit cell contact. HER2 disappeared from the membrane after 48 hours of shaking. **D**) Quantification
685 of the intensity signal of HER2 staining in Shaking-SKBR3 cells after 24, 48, and 72 hours. **E**) HER2 staining (Cy3)
686 in SKBR3 cells, seeded after 48 hours of shaking in LD condition and fixed after 6 hours. Quantification shows the
687 correlation between HER2 staining signal (Cy3) and DAPI in the nuclear and endoplasmic reticulum area (NER).
688 **F**) Mass spectrometric analysis identified desmosome junction components, particularly Desmoplakin (DSP) and
689 Vimentin (VIM), as consistent binding partners of HER2 across LD and HD conditions in MCF10A-teti-HER2_GFP

cells and shaking-SKBR3 cells. **G**) The physical binding of HER2 to Vim and DSP was further confirmed by co-immunoprecipitation in MCF10A-Teti-HER2-GPF cells treated with 1 µM Dox. **H-I**) Co-culture of MCF10A-teti-HER2_GFP cells with different cell types and tracking cell-cell contact and HER2 membrane localization. MCF10A-teti-HER2_GFP cells were cultured in LD condition for 24 hours and then co-cultured (in the same well as mixed culture) for an additional 24 hours with different cell types and extracellular matrix (ECM) conditions. Certain epithelial cell lines such as SKBR3 and MDA-MB453 could restore HER2 to the membrane, while others (such as HEK293T and SV80) did not exhibit this ability. The quantification represents the percentage of cell contacts overlapping with HER2 membrane localization in MCF10A-teti-HER2_GFP cells. **J**) mRNA expression of desmosome adhesion surface cadherin proteins, which show higher cadherin expression values for cells that can facilitate HER2 membrane localization in the co-cultures with MCF10A-teti-HER2_GFP. **K**) Upon siRNA knockdown of DSP in MCF10A-Teti-HER2-GPF cells, the total number of cells decreased in the KD group compared to the control (Scramble). This reduction in the number of cells appears to be due to a decreased cell junction ability in the DSP-KD group, as demonstrated in the right graph by increasing number of single cells in DSP-KD group. **L**) The intensity of HER2 and DSG2 decreased on the cell contact surface of cells upon the knockdown of DSP. Cells were fixed and stained for DSG2, 6 hours after culturing in the LD condition. P-values in panels B, D, E, and I were calculated using the Mann-Whitney U test, and data are presented as medians. P-values in panel K were calculated by the Student t-test, and data are presented as means ± SD. P-values in panel J were calculated using a One-way ANOVA test. P-values in panel L were calculated by the chi-square test.

Figure 4:

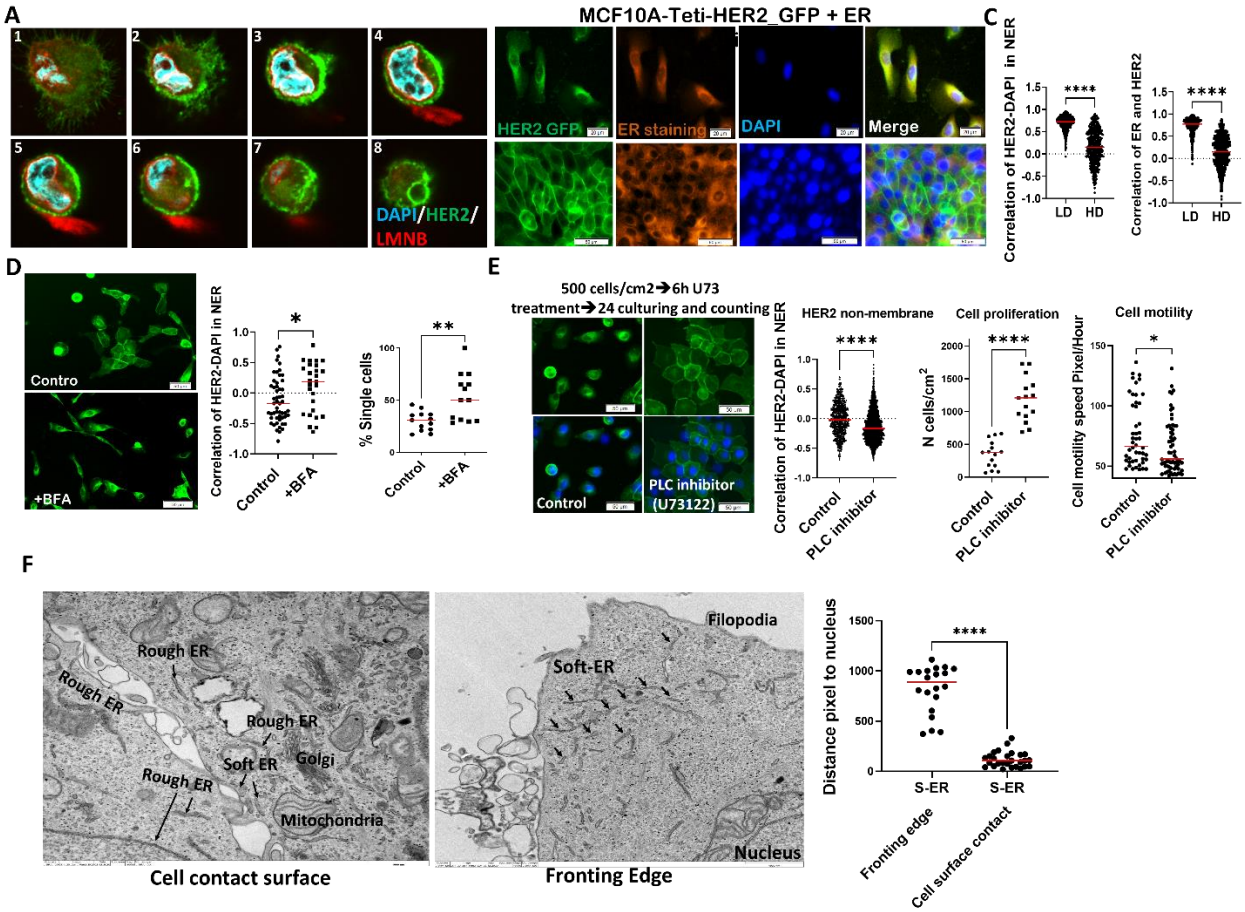

Figure 4: HER2 Accumulation in the Endoplasmic Reticulum (ER) due to a Shift in ER Function from Protein Trafficking to the Regulation of Cell Migration. A) Confocal imaging revealed the precise cellular localization of HER2. HER2 (FITC staining) was localized not within the nucleus (DAPI staining) but in close proximity to the nucleus. Notably, the nuclear envelope, comprised of a double membrane bilayer originating from the ER

membrane (indicated by LaminB1 staining in the Cy3 channel), forms the most evident boundary around the nucleus. **B**) A strong correlation between HER2 and ER was observed in low cellular density; however, this correlation is not seen in high density (HD). **C**) Quantification of HER2-DAPI in NER (nuclear and ER; right panel) and HER2 and ER in figure B. **D**) Inhibition of (anterograde) protein trafficking by BFA (50 µg/ml) increases the nuclear/ER localization of HER2 in MCF10A-teti-HER2_GFP cells, treated with 1 µM Dox and cultured in medium density (10000 cells/cm2). Quantification shows the increase in the NER and HER2 correlation upon BFA treatment and an increase in the number of single cells. **E**) Inhibition of ER function during cell migration by pharmacological inhibition of PLC. The MCF10A-teti-HER2_GFP cells, cultured in LD, were treated with 1 µM of PLC inhibitor for only 6 hours and then subsequently cultured for 24 hours. This treatment increases membrane HER2 localization (right quantification panel), increase cell proliferation (middle quantification panel; cell counting results), and decreases cell motility (left quantification panel). **F**) Transmission electron microscopy (TEM) imaging in MCF7 cells showed soft-ER moving alongside the leading edge of migrating cells and staying close to the nucleus in cells in compact structures, indicating changes in the organization of the S-ER upon changes in cell density. Arrows indicate different compartments of the cells in both conditions. All p-values were calculated using the Mann-Whitney U test, and data are presented as medians.

Figure 5:

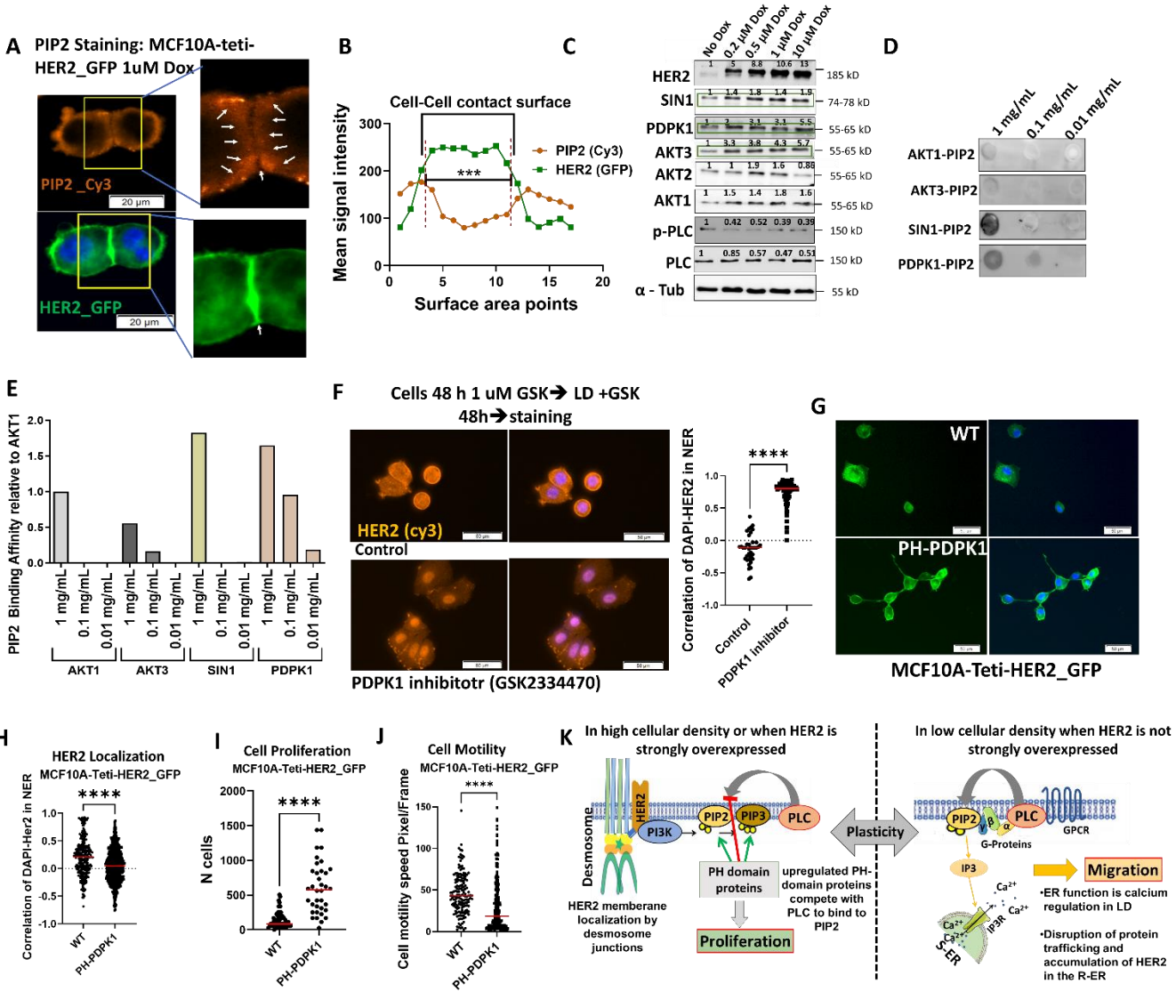

Figure 5: Molecular Switch: A Competition Between PLC and PDPK1 Defines Migration or Proliferation Phenotypes. A) PIP2 (Cy3) staining in MCF10A-teti-HER2_GFP cells treated with 1 µM Dox reveals a depletion of PIP2 at the cell-cell contact surface where HER2 localizes to the membrane. **B**) Quantification of PIP2 staining and HER2_GFP presented in Figure 5A. Intensity of Cy3 staining signal or GFP has been quantified across different areas of cell membrane. Results per each point show mean signal measured in 10 cells. **C**) AKT1, AKT3, PDPK1, and Sin1 PH domain proteins show co-upregulation in protein levels due to HER2 upregulation in MCF10A-teti-HER2_GFP cells treated with different concentrations of Dox. **D**) Protein lipid overlay (PLO) assay demonstrates that Sin1 and PDPK1 can bind to PIP2 at the highest concentration, with PDPK1 displaying a gradient of binding to varying PIP2 concentrations. **E**) Quantification of the PLO assay presented in Figure 5D. **F**) Pharmacological inhibition of PDPK1 rescues HER2 (Cy3) cellular localization in SKBR3 cells. **G-J**) Overexpression of the PH-domain of PDPK1 in MCF10A-teti-HER2_GFP cells cultured in LD reduces non-membrane HER2 (G, quantification in H), increases cell proliferation (I), and decreases proliferation (J). **K**) A molecular switch regulating cancer cell plasticity. Left: Upon cell-cell contact, HER2 localizes and stabilizes on the cell membrane by physically binding to desmosome proteins, thereby activating proliferation pathways through upregulation of the PH-domain-containing protein PDPK1. Activation of PI3K utilizes PIP2 to generate PIP3, and the upregulation of PDPK1 can also bind to PIP2, inhibiting the PLC pathway. Right: In LD, PLC can bind to PIP2, converting it to DAG and IP3. IP3 then binds to its receptor, IP3R, on the ER membrane, releasing Ca2+ and inducing migration pathways. All p-values are calculated using the Mann-Whitney U test, and data are presented by median.

Figure 6:

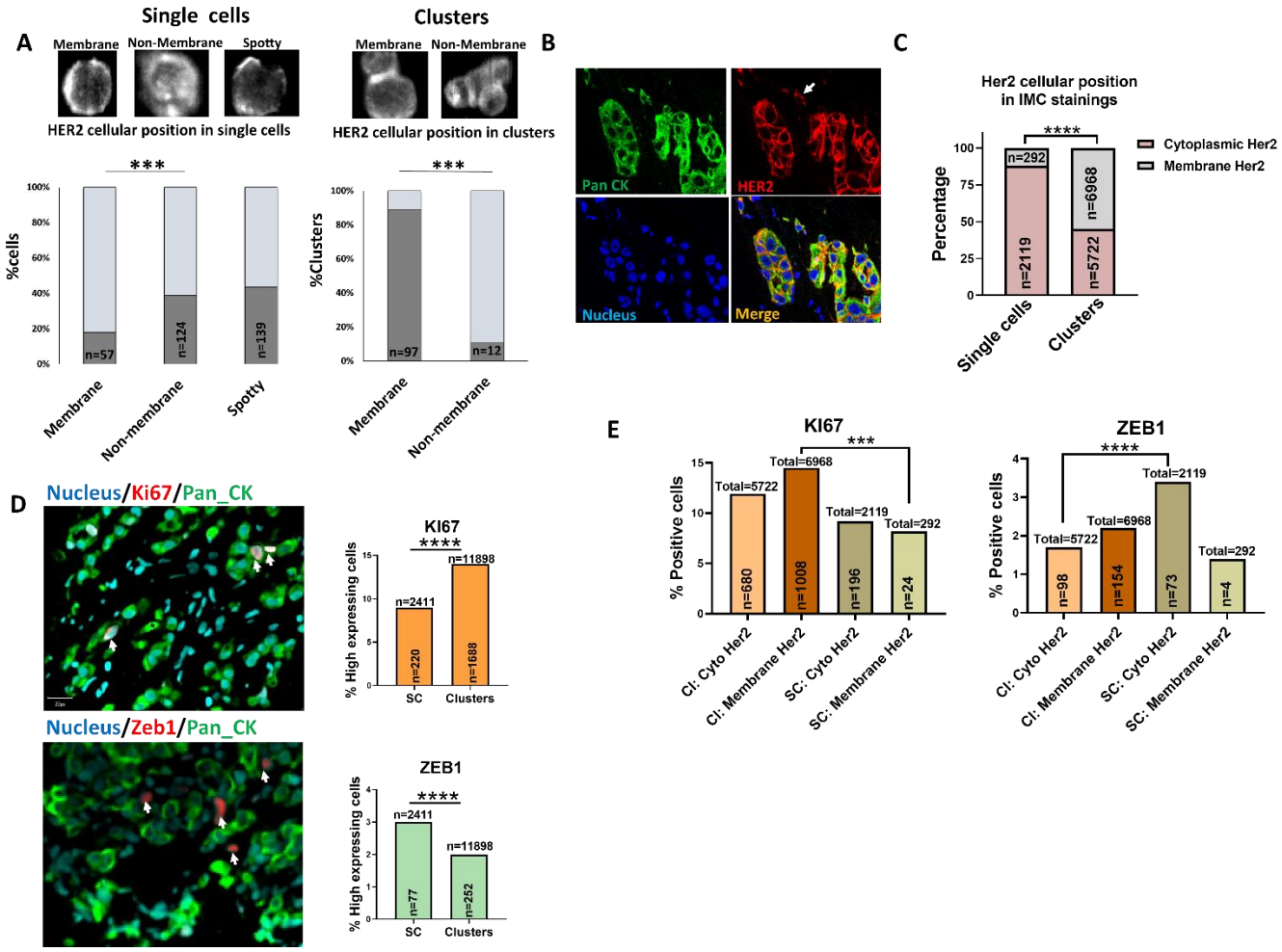

Figure 6: Clinical Relevance: Disseminated Cancer Cells in Breast Cancer Reduce Membrane HER2 and Transition from Proliferation to Migration Phenotype. A) Analysis of 429 circulating tumor cells (CTCs) and clusters obtained from 32 M1 (metastasis positive) HER2+ breast cancer patients using a cell search device to determine the cellular position status of HER2. Various examples of HER2 staining patterns are shown above the panel, with quantification presented below. Results indicate a higher prevalence of non-membrane HER2 staining in CTCs. In all HER2-positive clusters (89% of all clusters), HER2 staining is confined to the cell-cell contact surface of the cells. **B**) Results of imaging mass cytometer (IMC) staining for HER2 in 14 PT and metastasis human breast cancer samples. The arrow indicates non-membrane HER2 staining in solitary cells. **C**) Quantification of HER2 staining, distinguishing between membrane and cytoplasmic (non-membrane) staining of HER2. **D**) IMC staining examples for KI67 and ZEB1. On the right, quantification of KI67 and ZEB1 staining is presented, indicating a higher proliferation rate (KI67) in cluster cells and a more mesenchymal state (ZEB1) in single cells. **E**) Analyzing single cells and cluster cells to assess the HER2 cellular location in KI67 and ZEB1 positive cells. The number of KI67-positive cells with membrane HER2 staining is significantly higher in clusters compared to single cells (left panel). The number of ZEB1-positive cells with cytoplasmic HER2 staining is significantly higher in single cells compared to clusters (right panel). All p-values were calculated using chi-square test.

Supplementary Figures

Supplementary Figure 1:

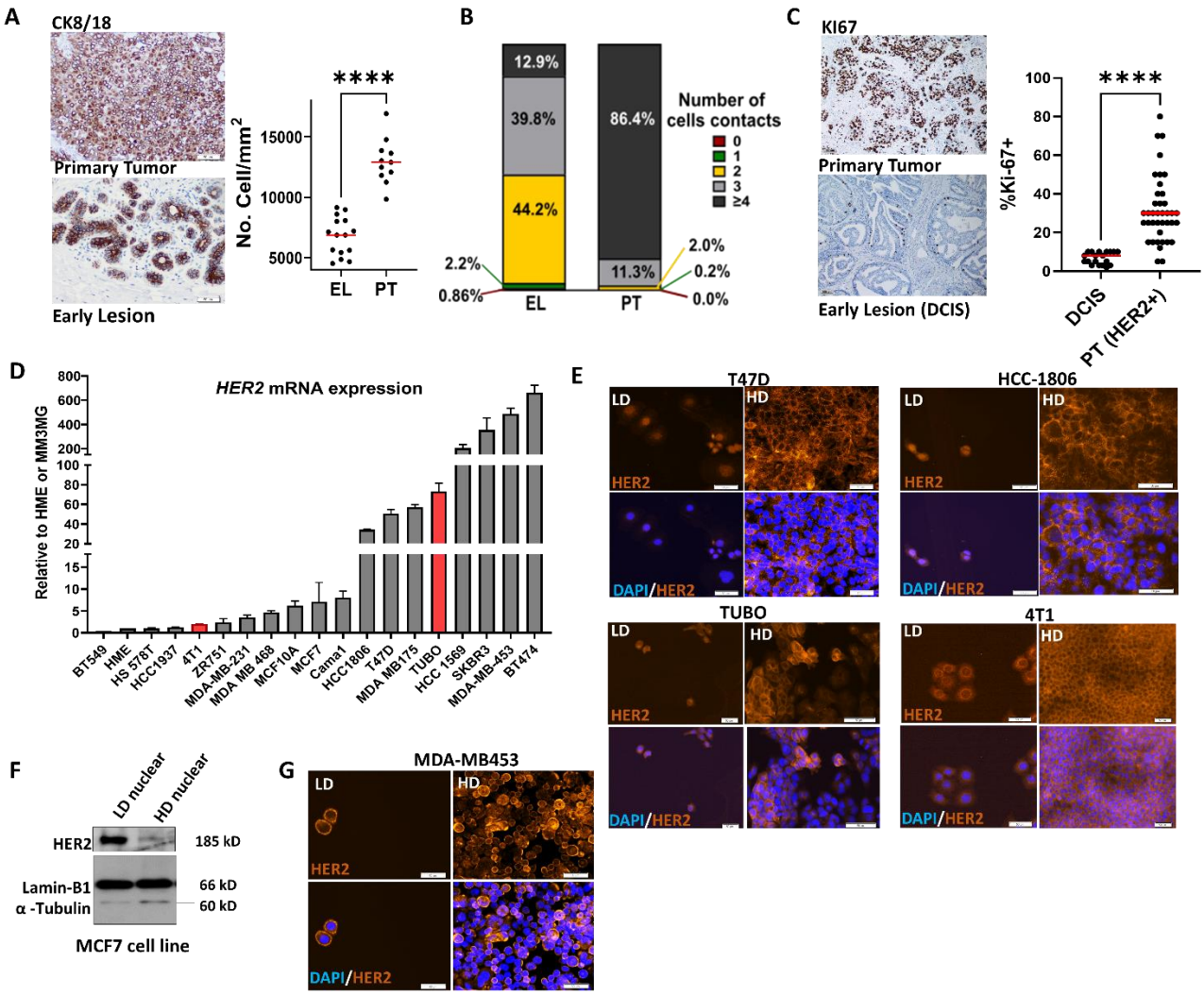

Supplementary Data Figure 1: Cell-cell contact and HER2 expression levels, and cellular density are linked to the membrane localization of HER2. **A**) Confirmation of tight epithelial structures in primary tumor (PT) compared to early lesion (EL) sections from human PT breast cancer samples, demonstrated through cytokeratin (CK8/18) staining. **B**) Quantification revealing a reduction in cell contacts within cells located in EL structures in contrast to those within PT structures of human PT breast cancer samples, presented as a percentage graph derived from counting cell contacts in five CK8/18 staining images per case. **C**) Elevated frequency of Ki67+ cells in PT's tight structures compared to EL in human breast cancer samples, indicative of higher proliferation levels. **D**) Relative mRNA expression levels of HER2 in various human breast cancer cell lines, in comparison to the hTERT-HME cell line (gray columns), and a murine breast cancer cell line, relative to the MM3MG murine mammary epithelial cell line (red columns). **E**) In cell lines with low to moderate HER2 expression, such as T47D and HCC-1806 (human cell lines), as well as TUBO and 4T1 (murine cell lines), HER2 localizes to the cytoplasmic-nuclear compartment at low cellular density (500 cells/cm2) but shifts to membrane localization at high cellular density (20,000 cells/cm2). **F**) Immunoblotting for the nuclear fraction of MCF7 cells in low density (LD) and high density (HD). Lamin B1 served as the loading control for the nuclear fraction, and α-Tubulin as the loading control for the cytoplasmic fraction. The absence of α-Tubulin in the nuclear fraction indicates the absence of cytoplasmic contamination in the nuclear fraction. **G**) In MDA-MB453 cells, a HER2+ cell line with strong HER2 expression, HER2 remains consistently localized in the membrane, irrespective of cell density. All p-values were

calculated using Student t-test; data in panels A and C are presented as means, and in panel D presented as means ± SD.

Supplementary Figure 2:

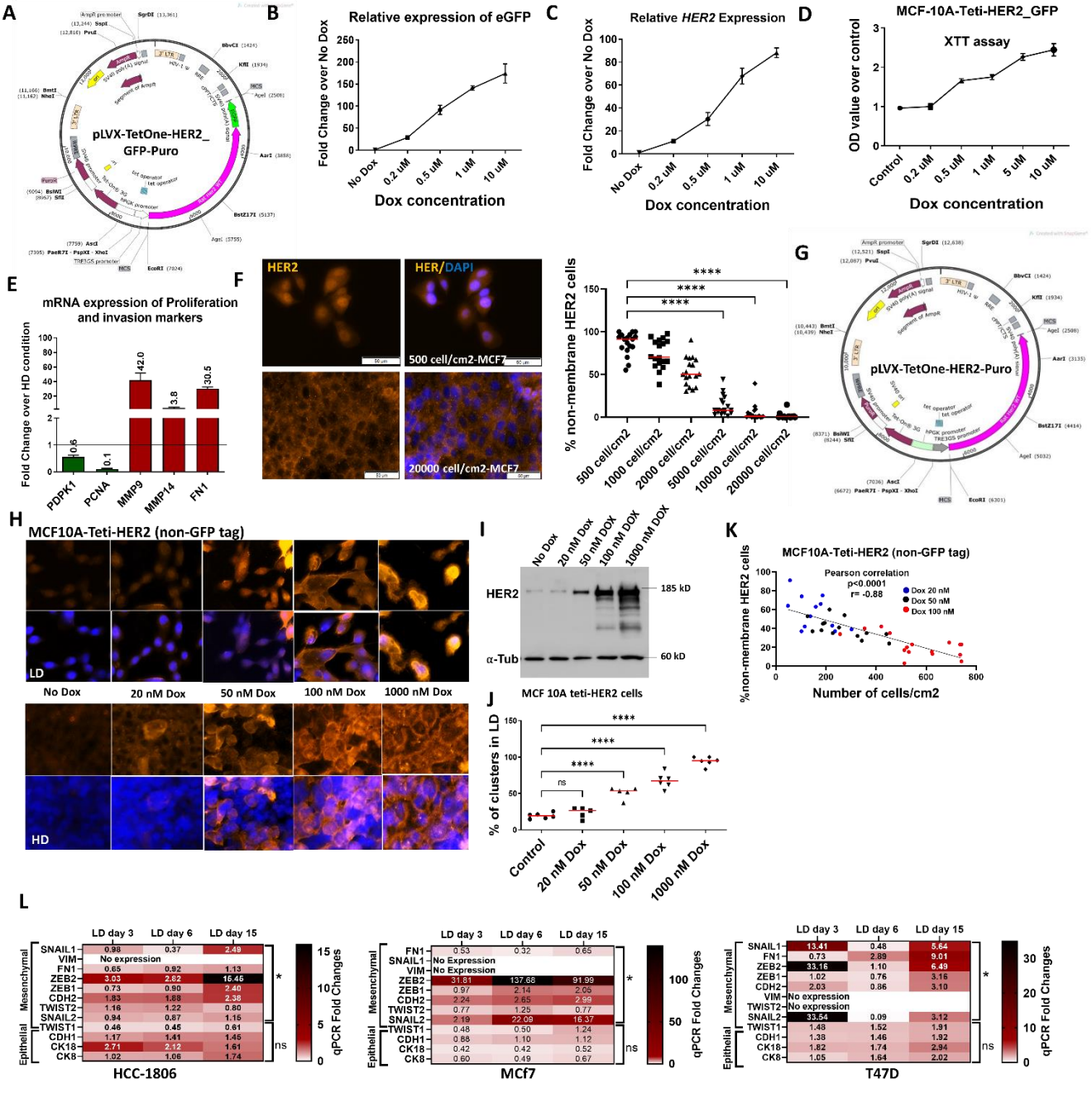

Supplementary Data Figure 2: HER2 Expression Level and Cell Density Regulation of HER2 Cellular Localization and Phenotypic State of Cells. A) A Tet-On HER2 inducible model in MCF10A cells. Addition of Dox induces HER2 expression, which can be tracked by GFP. **B-C**) The relative mRNA expression of eGFP (B) and HER2 (C) increases upon HER2 activation. In this model, administration of Doxycycline (Dox) induces HER2 expression that can be tracked by GFP. **D**) Inducing HER2 expression can increase cell proliferation in MCF10A-teti-HER2_GFP cells, as shown by the XTT assay measurement after 72 hours of treatment with different concentrations of Dox. **E**) Phenotypic switch in MCF10A-teti-HER2_GFP cells. mRNA expression levels of migration and proliferation markers at constant HER2 expression (1 µM Dox) under different densities cultured for 72 hours showed a

downregulation of Ki67 and PCNA (proliferation markers) expression but elevated MMP9, MMP14, and FN1 (invasion markers) levels in low-density (LD). **F**) In MCF7 cells cultured for 72 hours, increased cell density resulted in an increase in HER2 membrane localization. **G**) Map of the vector of a non-GFP-tagged MCF10A-Teti-HER2 model. **H-K**) This model in (G) was used to rule out the possible influence of the eGFP tag on HER2 function. The MCF10A-teti-HER2 cells were treated with different concentrations of Dox and stained for HER2 (Cy3) in LD and HD. Cells showed non-membrane HER2 localization in LD and membrane HER2 localization in HD, and upon Dox induction, the number of cells increased, while the percentage of non-membrane HER2 cells decreased. The non-GFP tag model is more Dox-sensitive compared to the GFP-tag model (J). Dox induction also resulted in more cluster formation in cells cultured in LD. **L**) Prolonged culturing of human breast cancer cells in LD conditions intensifies the induction of the mesenchymal state. The exception is T47D, which shows a reduction of mesenchymal genes on day 6; however, it significantly upregulates them on day 15. P-values in panel L were calculated using student paired t-test between day 15 and 3 days for HCC-1806 and MCF7 and between day 15 and 6 in T47D. P-values in panels F and I were calculated using the Mann-Whitney U test. The p-value in panel K is presented from the Pearson correlation test. Data in panels F and J are represented as medians, and data in panel E are represented as means ± SD.

Supplementary Figure 3:

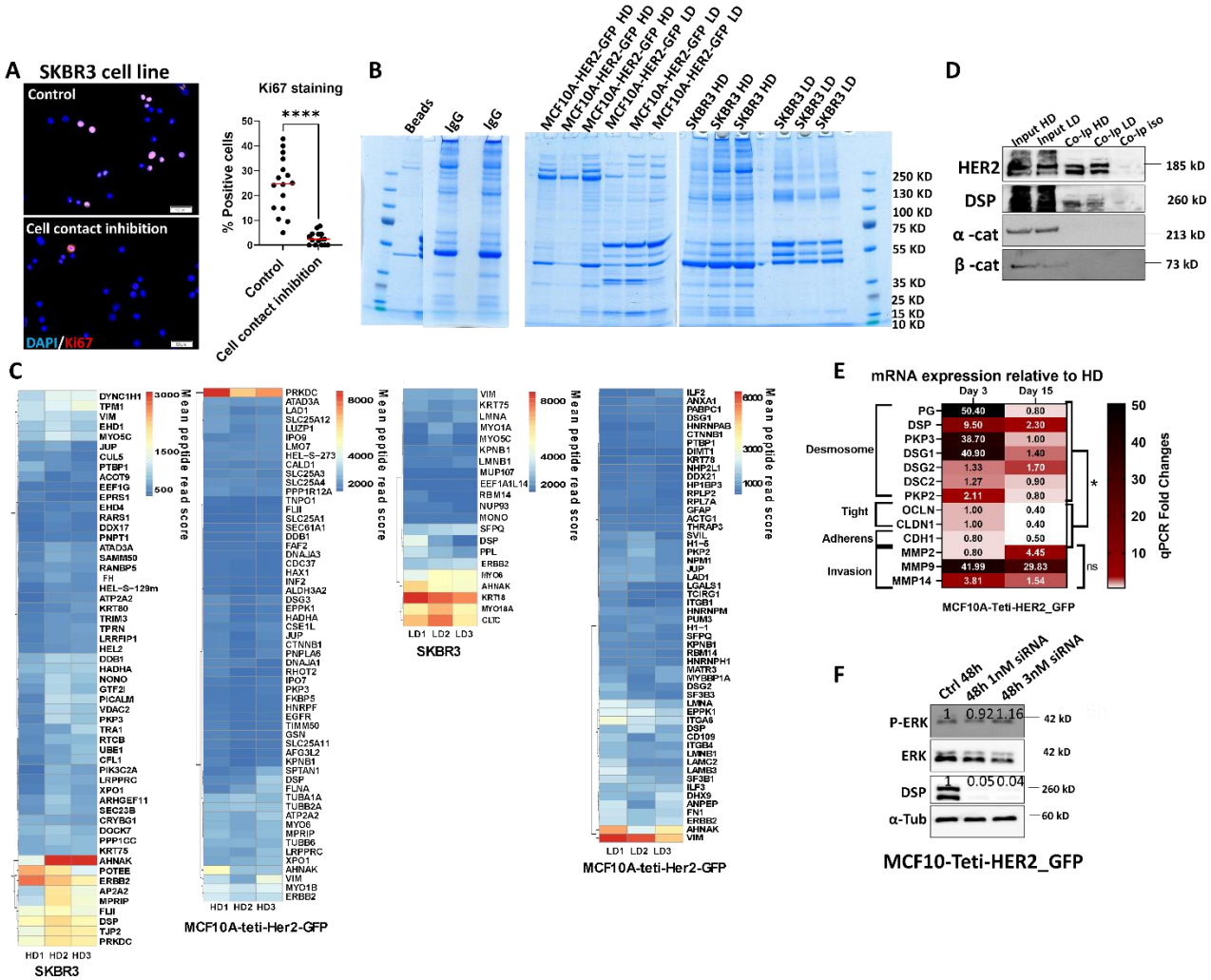

Supplementary Data Figure 3: Desmosome Junctions Initiate HER2 Membrane Localization in Early Cell-Cell Contacts. A) The frequency of Ki67+ cells were reduced in shaking-SKBR3 cells, confirming that the cytoplasmic localization of HER2 in SKBR3 cells reduced their proliferation ability. **B**) Image of the SDS-gel for mass spectrometry. **C**) Results of HER2 binding partners from protein mass spectrometry analysis for two cell lines and

LD and HD conditions. **D**) Co-immunoprecipitation of α-catenin and β-catenin with HER2. These two proteins do not physically bind to HER2. **E**) qPCR analysis of desmosome junctions in MCF10A-teti-HER2_GFP cells, treated with 1uM Dox and cultured in LD for 3 and 15 days. Desmosome junctions, compared with tight and adherent junctions, were upregulated after 3 days of being cultured in LD conditions and were the most stable cell junctions, gradually losing their expression profile during long-term culturing (15 days). **F**) Immunoblotting results of proliferation markers such as p-ERK in MCF10A-teti-HER2_GFP cells with DSP-KD showed that the knockdown had no effect on cell proliferation in HD. P-value in panel A calculated using the Mann-Whitney U test, and data presented as medians. P-values in panel E were calculated by the student t-test, and comparison applied for day 15 only.

Supplementary Figure 4:

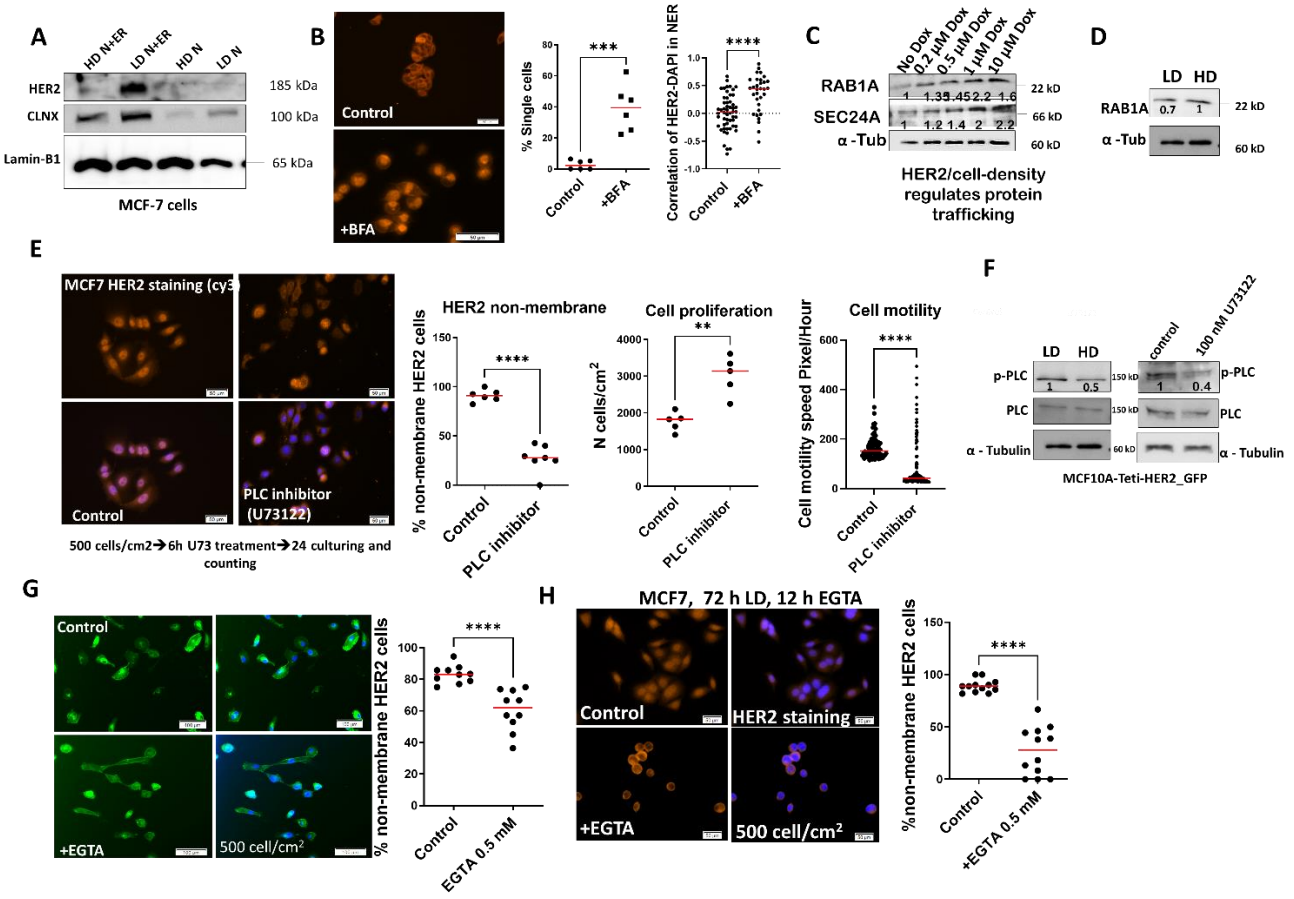

Supplementary Data Figure 4: HER2 Accumulation in the Endoplasmic Reticulum (ER) due to a Shift in ER Function from Protein Trafficking to the Regulation of Cell Migration. A) Immunoblotting of cell organelle fractionation in MCF7 cells. Also, refer to the methods section. The nuclear/cytoplasmic accumulation of HER2 (NER) correlates with the fraction enriched in calnexin (CLNX) protein, a typical marker for the ER organelle. **B**) Inhibition of (anterograde) protein trafficking by BFA (50 µg/ml) increases the nuclear/ER localization of HER2 in MCF7 cells cultured at medium density (5000 cells/cm2). Quantification shows the increase in the NER and HER2 correlation upon BFA treatment and an increase in the number of single cells. **C**) HER2 expression and cell density are the decisive factors for protein trafficking in cells. RAB1A and SEC24A, as two protein trafficking markers, are upregulated with an increase in HER2 expression and cell density in MCF10A-teti-HER2_GFP cells. **D**) The protein expression of RAB1A, a protein trafficking marker, is higher in HD than in LD in MCF10A-teti-HER2_GFP cells. **E**) MCF7 cells treated with 1 µM of PLC inhibitor for only 6 hours and subsequently cultured for 24 hours. This treatment increases membrane HER2 localization (right quantification panel), increase cell proliferation (middle quantification panel; cell counting results), and decreases cell motility (left quantification panel). **F**) Immunoblotting of PLC and p-PLC expression in LD is much higher than in HD in MCF10A-teti-HER2_GFP cells. Immunoblotting confirms PLC downregulation upon the addition of 100nM PLC inhibition (U73122). **G**) Calcium

withdrawal in MCF10A-teti-HER2_GFP cells, treated with 1uM Dox and 0.5mM EGTA. The treatment resulted in a lower percentage of non-membrane HER2 cells. **H**) Calcium withdrawal in MCF7 cells, treated with 1uM Dox and 0.5mM EGTA. The treatment led to a lower percentage of non-membrane HER2 cells. All p-values were calculated by the Student t-test, and data are presented as means.

Supplementary Figure 5:

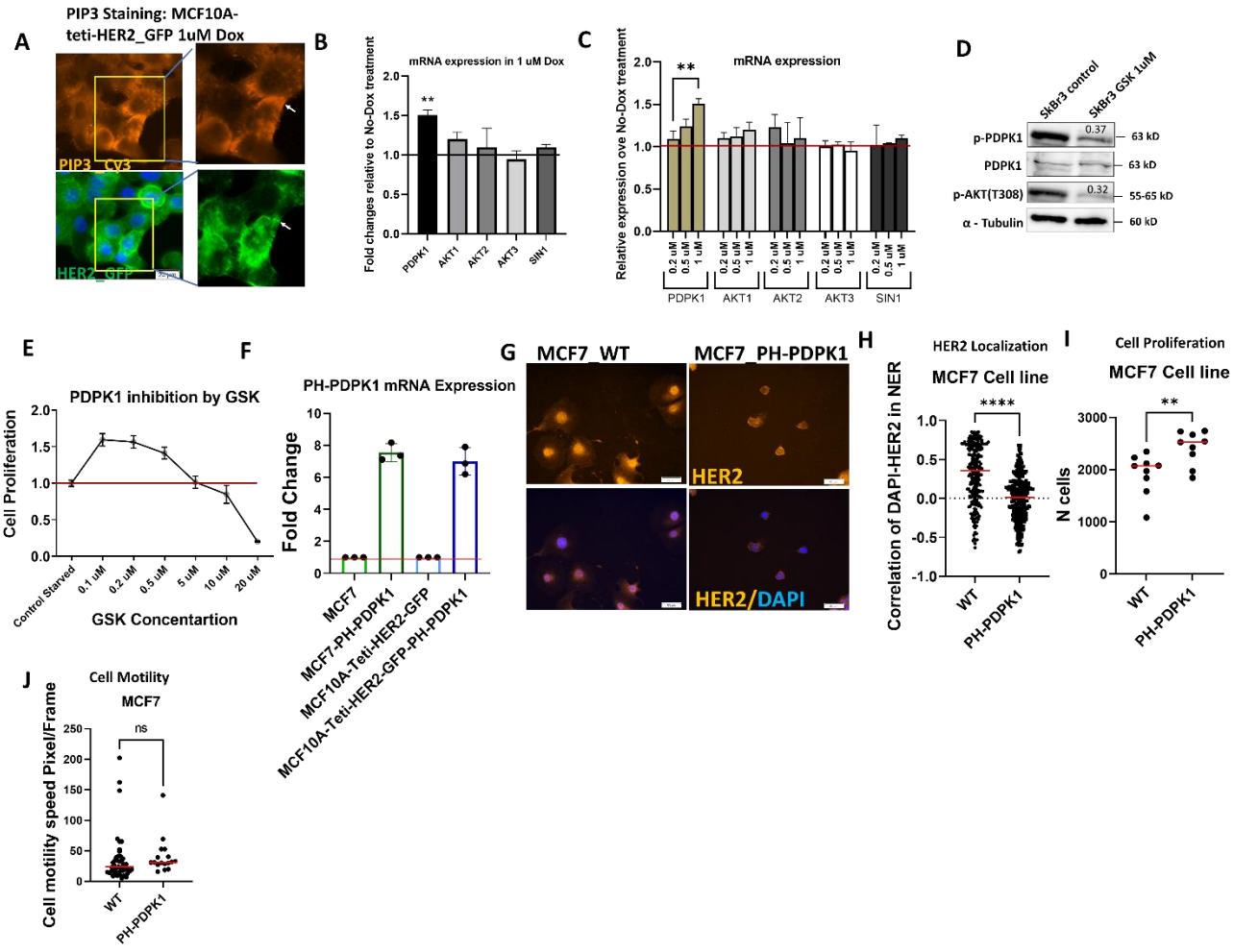

Supplementary Data Figure 5: Competition Between PLC and PDPK1 Defines Migration or Proliferation Phenotypes. A) PIP3 staining (Cy3) exhibits a strong correlation with HER2 at the cell-cell contact surface. **B-C**) qPCR analyses of genes encoding PH-domain containing proteins revealed that among all PH domain candidates, only PDPK1 was upregulated by HER2 levels in MCF10A-teti-HER2_GFP cells, displaying a HER2-dose-dependent expression pattern. **D**) Immunoblotting confirms PDPK1 downregulation upon treatment with the PDPK1 inhibitor (1uM) and its downstream target (p-AKT). **E**) Determination of the optimal concentration of the PDPK1 inhibitor, which inhibits proliferation while keeping the cells viable (relative quantification compared to the starved medium control). **F**) mRNA expression quantification of PH-PDPK1 overexpression. **G-J**) HER2 staining (Cy3) in MCF7 cells with overexpression of the PH-domain of PDPK1 (PH-PDPK1). PH-PDPK1 overexpression rescued membrane HER2 localization in LD (G and H) and increased cell proliferation (I). However, the impact of PH-PDPK1 overexpression on the cell motility trait of MCF7 cells was not detected, unlike what was observed for MCF10A-teti-HER2_GFP in Figure 5J (J). All p-values calculated using a student t-test, and data are presented by means.

Supplementary Figure 6:

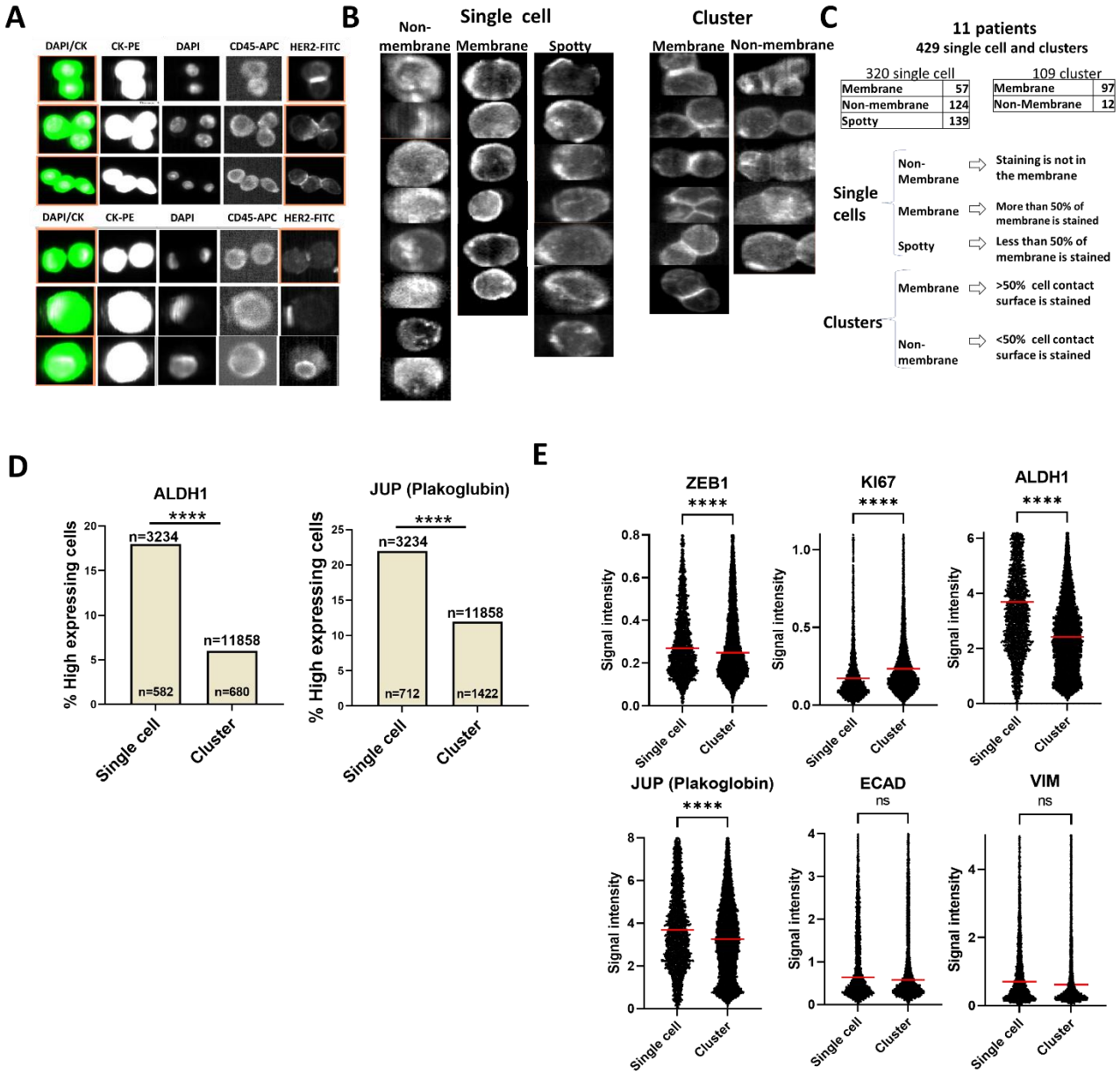

Supplementary Figure 6: HER2 Localization in Circulating CTCs, Clusters, and Solitary Cancer Cells in PT and Metastasis Lesions. A-C) Analysis of 429 circulating tumor cells (CTCs) and clusters obtained from 32 HER2+ breast cancer patients with metastases (M1) using a cell search device to determine the cellular localization status of HER2. Examples of CTCs and clusters with exclusive HER2 membrane staining on the cell-contact surface of clusters and nuclear HER2 staining in one cell (A). Various examples of HER2 staining patterns are shown in (B). Classification criteria for HER2 localization are shown in (C). **D**) Binary quantification of staining results of imaging mass cytometry (IMC) for ALDH1 and JUP show percentages of high expressing cells for these two proteins. **E**) Quantification of the staining signal for different markers used in IMC staining, including only CK-positive cells. All p-values were calculated using the Mann-Whitney U test, and the data are presented as medians.

Supplementary Methods and materials:

Cell lines, cell culture and cell stimulation:

Cell lines used in this study include 4T1 breast cancer cells, generously provided by Dr. Fred Miller from the Karmanos Cancer Institute in Detroit, MI. These cells originate from a spontaneous mammary tumour in a wild-type BALB/cfC3H mouse. The MM3MG mouse mammary epithelial cell line, derived from the BALB/c background, was procured from ATCC (ATCC® CRL6376™). Additionally, the TUBO cell line, a cloned cell line originating from a lobular carcinoma in a BALB-NeuT mouse, was a kind gift from Dr. Guido Forni at the University of Turin, Italy.

All mouse cell lines were cultured in DMEM medium (Anprotec:AC-LM-0011) supplemented with 10% fetal Bovine Serum (FBS (Pan Biotech: P40-37500)) (20% for the TUBO cell line), 2 mmol/L L-glutamine (Pan-Biotech: P04-80100), and 10 unit/ml penicillin/streptomycin (Pan-Biotech: P06-07050). Human cell lines were procured from ATCC and maintained according to ATCC's recommended culture conditions(MCF10A cells were cultured in DMEM F12(Anprotec:AC-LM-0018), supplemented with 2mM L-glutamine, 20ng/ml human Epidermal Growth Factor (hEGF(Sigma: E9644)), 100ng/ml cholera toxin(Enzo: BML-G117-0001), 10µg/ml bovine insulin(Sigma: I0516), 500ng/ml hydrocortisone (Sigma: H4001), 5% horse serum(Sigma: H1270) and 1% Penstrep. MCF7 and HCC-1806 cells were culture in RPMI 1640 medium (Anprotec:AC-LM-0060) supplemented with 10% FBS, 2 mmol/L L-glutamine (Pan-Biotech: P04-80100), and 10 unit/ml penicillin/streptomycin (Pan-Biotech: P06-07050). SKBR3, MDA-MB-231, MDA-MB-453, and HEK293T cells were cultured in DMEM High Glucose medium (Anprotec:AC-LM-0011) supplemented with 10% FBS (20% for the TUBO cell line), 2 mmol/L L-glutamine (Pan-Biotech: P04-80100), and 10 unit/ml penicillin/streptomycin (Pan-Biotech: P06-07050). The authenticity of the cell lines was verified through short tandem repeat (STR) analysis using Cell-ID™ (Promega).

Cultures were incubated at 37°C with 5% CO2 and were regularly screened for mycoplasma contamination, with all tests returning negative. Inhibitors, U73122(S8011), GSK 2334470(S7087), Brefeldin A(S7046) were obtained from Selleckchem, and their resuspension and preparation followed the manufacturer's instructions, with working concentrations as specified in the text. TGF-β (Transforming Growth Factor-β1; Peprotech: 100-21) was used in 5 ng/ml working concentration and was refreshed every 24 hours. For siRNA treatments, siRNAs were purchased from siToolsBiotec, and lipofectamine-based transfections were conducted in accordance with the manufacturer's protocols.

Cell density experiments:

All cell lines, with the exception of MCF10A, were cultured at a density of 20,000 cells/cm^2 for high-density experiments and 500 cells/cm^2 for low-density experiments. In the case of MCF10A, a seeding density of 2,000 cells/cm^2 was used for low-density experiments, while a density of 20,000 cells/cm^2 was employed for high-density experiments. All density-related experiments were conducted over a 72-hour period. For conditions requiring a shorter incubation time than our standard 72 hours (e.g., 24 hours), an increased initial seeding density was utilized to expedite the attainment of low and high cell densities, as mentioned in the results text.

Cell-Cell contact inhibition experiment:

The cells were dissociated and passed through 20 µm sieves and a total of 10^6 cells were cultured in 20 ml of DMEM high glucose medium within ultra-low adherent 15 cm plates, which previously had

been pre-coated with 1.2% poly-HEMA (Sigma: P3932). To prevent cell-cell contact, the plates were subjected to continuous shaking at 70 RPM and incubated at 37°C with 5% CO2 in a humid environment for a duration of 48 hours. Subsequently, 0.5 ml of medium containing the cell suspension was prepared for downstream experiments.

Transwell Invasion assay:

Transwell inserts (Corning: 3422) equipped with 8 µm pores were coated using a 40% Matrigel solution (Corning: 356231). A total of fifty thousand cells, sourced from tissue samples, were suspended in FBS-free medium before the seeding process. These cells were subsequently added to 200 µl of FBS-free medium (DMEM) on top of the Matrigel layer, while FBS medium (DMEM) was introduced into the lower chamber. After a 72-hour incubation period, the inserts were carefully removed, and were fixed by exposure to methanol at -20°C for 10 minutes, followed by staining with trypan blue. Enumeration of cells was performed by observing 3 fields (4x magnification) under a microscope.

Cell motility assay:

Time-lapse imaging with the incubator-microscope zenCELL owl: We performed live cell imaging using the 24-channel microscope zenCELL owl. This allowed us to monitor the different migration behaviour of cells in real time. Before starting cell monitoring, the culture medium was exchanged by fresh culture medium containing our target treatments. Cell motility was observed over 24 hours at 37°C and 5% CO2 using the zenCELL owl system with the following settings: total time lase imaging: 24 hours, interval: 10 minutes, exposure: 4, gain: 1, illumination: 43%, brightness: 58%. The recorded images of each experiment were processed and analysed as described in the following. MCF10A cells were cultured on the collagen surface treated plates (Roche 11179179001; 50 µg/ml, one hour coating). All cells were cultured 24 hours prior the start of experiment.

Image Analysis: Brightfield microscopy images captured from the zenCELL owl system for a period of 24 hours were analysed in our image analysis pipeline. Most of the images had varying background as well as foreground illumination. Therefore, any standard threshold-based segmentation algorithm did not work right out of the box. We used a two-stage segmentation method combining machine learning (ML) with a thresholding-based algorithm. Further, the first few frames from each well were excluded as they had significant background artifacts and illumination effects due to initial automated camera adjustment After segmentation, further post-processing on the segmented masks was done to remove cell debris, artifacts and cells touching the border of the image. Furthermore, in our analysis, we only kept cells that have a lifetime of at least 50 minutes, i.e., a cell should appear in 5 or more consecutive frames. By doing this, we were able to eliminate any remaining cell debris or artifacts that look very similar to a cell since most of these objects move very fast and they disappear from the camera frame. Finally, we used the cell segmentation masks as input to our cell tracking pipeline.

Cell segmentation in ilastik: We used the pixel classification workflow of ilastik [1] that assigns labels to pixels, based on pixel features and user annotations. In our workflow, we utilized various pixel features, such as pixel intensity, edge filters and texture descriptors at various smoothing levels. Once the features are selected, a random forest classifier is trained from user annotations. During the training process, annotations can be improved by using the live updates and results from the training process. In most cases, it was sufficient to train and annotate 1 to 2 images from each well depending on the variation of image illumination during the 24-hour time period. We did not use a trained image from one well to segment images of another well, as in most cases there was significant change in illumination and background artifacts per well. The workflow performs a semantic, rather than an instance segmentation and returns a probability map for each class, not individual objects. These probability maps are then processed by a threshold-based segmentation method in cellprofiler.

Cell segmentation in CellProfiler: We used the probability maps generated by ilastik and used a global threshold strategy on each image by applying the minimum cross-entropy algorithm in CellProfiler [2]. This provided us masks of each object from the images. To remove small cell debris from the probability maps, we applied a 30-to-90-pixel threshold depending on the background as minimum object diameter. We discarded objects that were touching the border of the image and subsequently filled up holes in the identified objects post thresholding. The object masks obtained from cellprofiler were then further processed in our cell tracking pipeline.

Cell tracking pipeline: We track cells by a greedy overlap labelling method using the Jaccard index between consecutive frames. The algorithm only looks in the forward direction of frames. This means that only the next frame is seen by the algorithm for cells with the most overlap to track its path. From the tracking algorithm, we get the x, y coordinates of the centre of mass of each cell. We also measure morphological features like eccentricity, area and perimeter of each tracked cell for further analysis. Once all the measurements are extracted, the average speed and total distance covered by each cell are evaluated. We then compared control cell lines with treated cell lines by assessing the 20% fastest moving cells between the two conditions. Thresholds like minimum number of frames a cell should appear and per cell area were applied to get results from the most reliable cells depending on presence of cell debris and background artifacts. In order to only compare moving single cells between control and treatment conditions, we exclude objects having a large area to remove clusters of cells, mostly resulting from cell division.

Protein Mass Spectrometry:

Mass spectrometry was essentially done as described previously (*1*). In summary proteins were separated using a 4%–12% NUPAGE Bis-Tris gel with MOPS buffer and stained with Simply Blue colloidal Coomassie blue G250. For mass spectrometric (MS) analysis, the gel lane was cut into slices, washed with various solutions, and lyophilized. Cysteines were blocked with DTT and iodoacetamide, followed by in-gel trypsin digestion. Peptides were eluted and reconstituted in 1% formic acid for LC-MS/MS analysis on an UltiMate 3000 RSLCnano System coupled to a maXis plus UHR-QTOF System. Data-dependent acquisition of MS/MS spectra was performed, and raw data processing involved database searching of the UniProtKB/Swiss-Prot Homo sapiens database with specific parameters for enzyme specificity, modifications, and tolerance values. Protein identification was facilitated using software tools.

Proliferation assay:

For the XTT assay, single-cell suspensions were cultured in 96-well plates (Corning Inc., Corning, NY, USA), and cell proliferation was assessed using the XTT colorimetric assay kit (Roche: 11465015001), following the manufacturer's instructions. The cell seeding density was 10000 cells/well, and the experiment included 6 technical replicates. Media were supplemented with the relevant experimental factors, inhibitors, or vehicle and were refreshed every other day.

Given the limited sensitivity of XTT and several other commercial kits in detecting variations in cell numbers under our low-density conditions, we opted to employ a straightforward cell counting method utilizing ImageJ cell counter plugins.

Immunohistochemistry:

For CK and HER2 immunohistochemistry staining in tissue, 5 µm sections of paraffin blocks were mounted onto poly-L-lysine-coated slides. The samples underwent dewaxing via two 5-minute washes in xylene, followed by rehydration through graded alcohol with 5-minute wash steps and a final rinse

in water. Antigen retrieval was carried out using a standard Tris-EDTA buffer and pressure-cooking. Subsequently, sections were blocked with 0.3% H2O2 in TBS and 10% normal goat serum.

Sections were then subjected to a 1-hour incubation with the primary antibody, followed by the addition of a secondary antibody (Vector lab: PK4001 or PK5000), as per the manufacturer's recommended dilution (refer to AB table 2). After PBS washing, the ABC detection system (Vector laboratory) was employed in accordance with the manufacturer's instructions. Visualization was achieved using a chromogen reagent (Dako: 10046560) following the manufacturer's guidelines.

To quantify stained cells, the QuPath software was utilized, particularly its IHC positive staining function. Furthermore, QuPath facilitated the measurement of CK staining cell density across the stained area, a procedure carried out for EL and PT samples. For assessing cell contact numbers, five representative CK staining images were generated for each condition, and cell contacts were manually counted.

Immunofluorescence (IF) staining:

For staining of cells from monolayer cell culture, cells were initially seeded in 24-well culture plates at an appropriate density. Following a 72-hour incubation period, the cells underwent washing with PBS 1x and were subsequently fixed using 4% PFA for 10 minutes and washed twice with PBS 1x. The cells were then permeabilized with 0.3% Triton X-100 (Sigma: T8787) in TBS, followed by additional washing steps by TBS 0,1% Triton X-100 and blocking with Goat Serum (DAKO #315) in TBS 0,1% Triton X-100at room temperature. Next, the cells were incubated with the primary antibody (please refer to Supplementary Table 3 for details) for 1 hour at room temperature. Afterward, the cells underwent three washes with TBS 0,1% Triton X-100and were subsequently incubated with labelled secondary antibodies (Jackson ImmunoResearch Laboratory Inc) for 1 hour at room temperature. For nuclear counterstaining, the cells were incubated for 10 minutes with DAPI at a concentration of 0.5 µg/ml (Sigma: 28718-90-3).

For staining of cells attached to the inserts from invasion experiments, inserts were used immediately after migration (as described in the section detailing the invasion assay). The staining process, including the blocking step and immunofluorescence staining, was carried out similar to the monolayer cell culture staining procedure.

All images were captured using an AxioVert 200M microscope (Carl Zeiss Microscopy). Additionally, for ER staining, the CytoPainter-ER Staining kit (ab139482) was employed, following the instructions provided by the kit manufacturer.

Protein lipid overlay assay (PLO):

A Protein Lipid Overlay (PLO) assay was conducted to assess the binding interactions between various lipid molecules, including PIP2, and specific proteins labeled with HIS tags. Commercially available PIP2 was bought from Sigma-Aldrich 850155P in dry powder and dissolved in chloroform/methanol/water (20:9:1, v/v) (CMW solution) at a concentration of 1 mg/mL. Lipid spots containing PIP2were prepared at different concentrations (0.01, 0.1, and 1 mg/ml) on a polyvinylidene fluoride (PVDF) membrane and dried at room temperature for 30 to 60 min. The membranes were blocked with fresh sterile-PBST blocking buffer (0.1% Tween 20, v/v + BSA 3% (sterile BSA), m/v in PBS) for 1h in RT. Peptides, including ATK1 and AKT3 (biotrend), Sin1 (Biotechne), PDPK1 (MRC PPU reagent), all labeled with HIS tags, were prepared in similar concentrations in sterile water and the membranes were incubated with

2 ml peptide solution at 4 °C overnight. Following incubation with the proteins, membranes were washed four times with fresh PBST for 10 min each time. Detection was achieved using His-HRP (1:2000) in fresh sterile-PBST for 1 hour at room temperature antibody. Lipid-binding proteins bound to the membrane were detected by enhanced chemiluminescence (ECL) according to the manufacturer's instructions.

Cell Fractionation:

Isolating the Cytoplasmic Fractionation: To begin, cells were resuspended in lysis buffer containing Tris ultrapure: 50 mM (0.61 g), EDTA: 5 mM (1.86 g), NaCl: 137.5 mM (0.8 g), Igepal-CA630: 1% (1 ml), Glycerol: 5% (5 ml). The supernatant from the cell suspension carefully transferred to a fresh tube, leaving a small volume behind to prevent nuclear contamination. This initial supernatant is then centrifuged at low speed and low temperature, allowing the cytoplasmic fraction to settle at the bottom. The supernatant is transferred again, with another small volume reserved, and subjected to a higher-speed centrifugation for an extended duration. This step results in the primary cytoplasmic fraction.

Nuclear Fraction Purification: The nuclear pellet the subjected purification process involves multiple elegant washing and mild centrifugation steps aimed at removing contaminants and enhancing the purity of the nuclear material. The nuclear material is then subjected to sonication and incubation on ice. This treatment is designed to release the nuclear and ER (Nuclear Envelope + Endoplasmic Reticulum) fraction. After the appropriate incubation period, one sample is designated as the Nuclear + ER (NER) fraction, while another is centrifuged to obtain the nuclear fraction in its purified form. Please note that a detailed bench protocol with precise quantities and instructions will be provided upon request.

Quantitative PCR:

All mRNA extractions were performed using RNeasy kit (Macherey-Nagel:740955.50) according to manufacturer's instructions. cDNA was generated using reverse transcriptase kit (ThermoFisher: k1622). Finally, 5 ng of cDNA was used for qPCR. Quantitative PCR was performed using a LightCycler instrument (Roche) and Fast Start Master SYBR Green Kits (Roche). Data analysis was done using the RelQuant software (Roche) with a reference gene and a calibrator (reference) sample in every run. Mouse and human reference cDNA served as a positive control. Measurements that showed unspecific products in the melting curve analysis were discarded from further analysis. Expression levels are given relative to *Actb* (β-actin) for gene expression analyses (primer sequences are provided in Table 3). All primers were synthesized by Eurofins MWG Operon, Germany.

Lenti- and retroviral transduction:

Overexpression, including shRNA, PH-PDPK1, PLC, and DSG2 expressions, were accomplished through lentiviral constructs obtained from Vector Builder, utilizing a pLV-expression-based system. For the tet-inducible model, a custom construct was created based on the pLVX-TRE-IRES-Puro backbone (vector maps are provided in the figures for Tet-inducible constructs). Lentiviral packaging followed previously established protocols(*2*), with helper vectors pSPAX2 and pMD2.G (Addgene). Selection of transduced cells was carried out using the selective antibiotics with proper concentration for each cell line. MCF10A-teti-Her2_GFP cells with 10 µg/ml of puromycin (Sigma Aldrich: P8833), MCF10A-teti-Her2_GFP, MCF7, and SKBR3 with 150, 500 and 1000 µg/ml of G418 (Sigma Aldrich: G9516) respectively. MCF10A-teti-Her2_GFP and MCF7 with 200 and 400 µg/mL of hygromycin (Sigma H9773) respectively.

For the inducible model, Doxycycline (Sigma D9891) treatments were administered every two days, with fresh medium containing Doxycycline used at various concentrations depending on the experimental objectives.

Western blot analysis and Co-immunoprecipitation (Co-IP):

Cell lysis was performed by resuspending cells in a lysis buffer containing the following components: Tris ultrapure (0.61 g, 50 mM), EDTA (1.86 g, 5 mM), NaCl (0.8 g, 137.5 mM), Igepal-CA630 (1 ml, 1%), and Glycerol (5 ml, 5%), with a 30-minute incubation on ice. Protein extraction was achieved through centrifugation at 14,000 RPM. The resulting supernatant, containing the extracted proteins, underwent quantification using the BCA protein assay kit (Thermo Scientific: 23227) to ensure uniform protein concentration.

Subsequently, the quantified protein lysates were separated on different percentages of SDS-PAGE gels, depending on the size of the target protein, transferred onto PVDF (Millipore, Billerica, MA, USA), and subjected to immunoblotting using primary antibodies overnight. Following this, horseradish peroxidase-conjugated secondary antibodies were applied. Visualization of protein bands was accomplished using enhanced chemiluminescence (ECL) according to the manufacturer's instructions, and bands were detected using Imagequant LAS 4000 (GE Healthcare).

For Co-IP experiments, the Crosslink IP Kit (26147 Pierce™ Crosslink IP Kit) was employed following the manufacturer's instructions. Initially, 10 µg of the antibody was coupled with resin slurry, and the resin was washed with Coupling Buffer. After confirming successful antibody coupling, the resin was further washed, and a crosslinking solution was prepared and added to chemically attach the antibody to the beads using DSS solution. Following the crosslinking reaction, the resin was washed again, and immunoprecipitation was carried out.

Imaging Mass Cytometry (IMC):

TMA section including 14 FFPE PT and metastasis samples from 6 M1 breast cancer patients with HER2 positive PT status (Table1) was cut in 5 µm slides. Samples were collected based on consent form approved by ethics committee (Ethics vote Numbers: 07-079 V1, 07-079 V2, 17-672-101 V2) of the University of Regensburg. These slides baked for 2h at 60˚C prior to tissue pretreatment and antigen retrieval in Ventana Discovery Ultra Platform (Ventana Medical Systems Inc. Tucson, Arizona, USA). After pretreatment in Ventana, the TMA section was first washed 3 times in warm soap water and again 3 times in clean warm water to remove LCS (liquid cover slip (650-010), Roche Diagnostics GmbH, Manheim, Germany). Following this, tissue was blocked for 45 min at RT in a humidity chamber using blocking solution (3% of BSA solution in phosphate saline buffer (PBS)) and then stained using an antibody cocktail overnight in a humidity chamber at 4˚C. The antibody cocktail consisted of anti-PanKeratin antibody (clone AE-1/AE-3, 1:800, Standard BioTools, San Francisco, CA, USA), anti-vimentin (clone D21H3, 1:400, Standard BioTools), anti-gamma-catenin (clone 15F11, 1:100, BioLegend, San Diego, California, USA), anti-ALDH1 (clone 44/ALDH, 1:100, Bd Bioscience, San Jose, California, USA), anti-E cadherin (clone 24E10, 1:200, Standard BioTools), anti-HER2 (clone D8F12, 1:150, Cell Signaling Technology, Danvers, MA, USA), anti-Ki67 (clone B56, 1:100, Standard BioTools), and anti-Zeb1 (clone E2G6Y, 1:50, Cell Signaling Technology) dissolved in 0.5% BSA PBS solution. After incubation overnight, the slide was washed two times using a PBS solution of 0.2% Triton x-100 (Sigma-Aldrich, Saint-Louis, Missouri, USA) for a duration of 8 min and then again for another 8 min using MiliQ water. After the wash, nuclear staining was performed using the iridium intercalator diluted in PBS (1:4000, Standard BioTools) for 30 min at RT. Following nuclear staining, the slide was washed for 5

min in MiliQ water and air dried for at least 20 min at RT before image data were acquired using a Hyperion Imaging System (Standard BioTools).

IMC data analysis:

Obtained IMC data were first pre-processed as previously described by Windhager et al. (10.1101/2021.11.12.468357) in order to obtain .tiff files which were then corrected for signal spillover as described previously(*3*) . The prepared image datasets were then loaded in QuPath for further analysis(*4*). To simplify the analysis process, tiff images were first stacked using a Python script to consist of only those channels in use for each analysis session. In the first session, HER2, PanKeratin, and iridium channels were used. Cell segmentation was performed on the base of the signal in the iridium channel by using a built-in cell detection function, and then the object classifier was trained using HER2 and PanKeratin channels and cell measurements (area, perimeter, eccentricity, minimal and maximal perimeter, and nucleus/cell area ratio) in order to detect 5 different cell types (solitary cancer cells with HER2 localized predominantly on the membrane and in the cytoplasm, clustered cancer cells with HER2 localized predominantly on the membrane and in the cytoplasm, and non-cancer cells). Annotations were exported in the form of GeoJSON files and used in the second session together with stacked tiff files consisting of the rest of the channels (E-Cadherin, Vimentin, ZEB1, ALDH1, KI67, and Gamma-catenin). In the second session, the mean signal intensity was measured for each of the channels, and as the measurements were performed on the top of annotations from the first session, also for each of the cell types identified in the first session. The obtained data was capped using an R script to remove the outliers. In order to divide cells based on the ZEB1 and KI67 expression as positive or negative for these markers, staining intensity was manually evaluated for each image in order to determine individual thresholds. This step was performed in the third QuPath session, using a single measurement classifier, where the patterns of positive cells were followed in real-time while adjusting the threshold values for each marker and compared with real staining. These thresholds were then used in R script to binarize the KI67 and ZEB1 intensities into ZEB1 and KI67 positive and negative cell populations that were then used in further analysis. The images were prepared for visualization by using IMC denoise pipeline as described in work by Lu et al(*5*).

Bioinformatic and Statistical analysis:

Statistical analyses and assessment of data variation within each dataset were conducted using GraphPad Prism V9.5. All in vitro and primary culture experiments were independently performed at least in three replicates, and comparisons were carried out using the student's t-test. Pearson correlation tests were employed to assess correlations between traits depicted in graphs. When comparing numerical values across different groups, Fisher's exact or chi-square tests were utilized.

To determine the appropriateness of parametric or non-parametric tests, D'Agostino normality tests were conducted. For assessing mean differences among groups of three or more, Anova tests were applied. All p-values presented in the figures and legends are two-tailed. Correlation analyses involving different staining were executed using CellProfiler (V4.2.1) software, and detailed pipelines and example images are available upon request.

References

1. D. Hasler *et al.*, The Alazami Syndrome-Associated Protein LARP7 Guides U6 Small Nuclear RNA Modification and Contributes to Splicing Robustness. *Molecular cell* **77**, 1014-1031.e1013 (2020).
2. S. A. Stewart *et al.*, Lentivirus-delivered stable gene silencing by RNAi in primary cells. *Rna* **9**, 493-501 (2003).
3. S. Chevrier *et al.*, Compensation of Signal Spillover in Suspension and Imaging Mass Cytometry. *Cell systems* **6**, 612-620.e615 (2018).
4. M. P. Humphries, P. Maxwell, M. Salto-Tellez, QuPath: The global impact of an open source digital pathology system. *Computational and structural biotechnology journal* **19**, 852-859 (2021).
5. P. Lu *et al.*, IMC-Denoise: a content aware denoising pipeline to enhance Imaging Mass Cytometry. *Nature Communications* **14**, 1601 (2023).

Supplementary Table 1: List of human patient samples used for IMC analyses.

PT/Met matched	ID-Nummer	ample type
1	1	Peritoneum cell pellet
1	2	Bladder Met
2	3	Skin Biopsy
3	4	Mammary Punch
3	5	LN
3	6	Axillary Met
3	7	Pericardial
3	8	Pleural Effusion
4	9	Mammary Biopsy
4	10	LN
5	11	LN
5	12	Pleural Effusion
6	13	LN
6	14	PT

Supplementary Table 2: List of Antibodies

Antibody	Company (Cat-Nr)	Conc for WB
DSP	Proteintech 25318-I-AF	1:200
Phospho Her2	Affinity AF3069	1:500
HER2	Cell Signal 2165	1:250 WB, IF, IP
HER2	Thermofisher PA516305	1:250 WB, IF
Her2	Thermofisher MA5-15050	1:100 IF
Phospho PLC	Cell Signal 2821S	1:200 WB
PLC	Cell Signal 5690S	1:250 WB
E-Cadherin	BioLegend 8866702	1:250 WB
Lamin-B	Proteintech 66095-I-Ig	1:5000 WB, 1:200 IF
Phospho PDK1	Cell Signal 3061S	1:500 WB
PDK1	Cell Signal 3062S	1:250 WB
Phospho AKT	Cell signaling 4060	1:250 WB
Tubulin	Sigma T9026	1:10 000 WB
Vimentin	Cell Signal 5741S	1:500 WB
Total AKT	Cell signalling 2920	1:2000 WB
β-Actin	Sigma Aldrich A5441	1:5000 WB
Erk1/2	Cell signalling 4695	1:1000 WB
p-Erk1/2	Cell signalling 9106	1:1000 WB
AKT1 AKT2 AKT3 Pan-AKT	Cell signalling 2938 Cell signalling 3063 Cell signalling 8018 Cell signalling 4691	1:1000 WB 1:1000 WB 1:1000 WB 1:1000 WB
Sin1	Cell signaling 12860S	1:1000 WB
Phospho-Sin1	Cell signaling 14716S	1:1000 WB
Rab1A	Cellsignaling D3X9S	1:125 WB
Calnexin	Proteintech10427-2-AP	1:4000 WB
N-cadherin	Proteintech 22018-1-AP	1:5000 WB
Sec24A	Invitrogen PA5-100110	1:1000 WB
Phospho PLC gama1	Cellsignalling 8713	1:1000 WB
DSC2	Proteintech	1:1000 WB, 1:200 IF
Alpha-catenin	Thermofisher	1:250 WB
Beta-catenin	epitmics	1:125 WB
Anti-Mouse IgG Peroxidase	Sigma A8924-.5ML	1:3000 WB
Anti-Rabbit IgG Peroxidase	Sigma A0545-1ML	1:5000 WB
KI67	Thermofisher MA5-14520	1:250 WB, IF
DSG2	Proteintech 21880-1-AP	1:250 WB, IF
PIP2	Echelon Biosciences Z-P045	1:100 IF
PIP3	Echelon Biosciences Z-A345	1:100 IF
Anti-His-tag-HRP	Proteintech HRP-66005	1:1000 WB

1309

1310 Supplementary Table 3: List of qPCR primers:

Name	Sequence For	Sequence Rev	Species
PDK1	GAAGCAGTTCCTGGACTTCG	ACCAATTGAACGGATGGTGT	human
AKT1	TCTATGGCGCTGAGATTGTG	CTTAATGTGCCC GTCCTTGT	human
AKT2	TGAAAACCTTCTGTGGGACC	TGGTCCTGGTTGTAGAAGGG	human
AKT3	TGAAGTGGCACACACTCTA ACT	CCGCTCTCTCGACAAATGGA	human
Sin1	CAGGACAGACTGCTGCCAATGA	GGCAGTAGGCACTGACATTGTC	human
PCNA	TCCTCCTTCCCGCCTGCCTGTAGC	CGCGTTATCTTCGGCCCTTAGTGTA	human
Ki67	TGAAGATGCAGCTGACTCTG	AGCACTCTGTAGGGTCGAG	human
Cdh1	TGATTTTTCGGCAGTTCAAGC	ACAATTATCAGCACCCACACA	human
CK 18 III	TATCACACGACTGCAGCTGG	GATGTCTGCCATGATCTTGG	human
CK 18	GTTCTGCAGATTGACAATGCC	GTCATCAATGACCTTGCGGA	human
Krt8	GATCTCTGAGATGAACCGGAACA	GCTCGGCATCTGCAATGG	human
Cdh2	TGGGAATCCGACGAATGG	TGCAGATCGGACCGGATACT	human
Zeb1	GAAAAACCACAAGGGGATGAG	GCTTGACTTTCAGCCCTGTC	human
Zeb2	CCTGCTACTTTCATGCCACC	CCATCAAGCAATTCTCCCTGA	human
Snail 1	CTGCCAATGCTCATCTGGGACTCT	TTGAA GGGCTTTCGAGCCTGGAGAT	human
Snail2	ACATGTCGGTTGTCTGGTTG	CGCCAGGAATGTTCAAAGCT	human
TWIST 1	CAGCGCACCCAGTCGCTGAA	CTTGTCCGAGGGCAGCGTGG	human
TWIST2	AGCAAGAAGTCGAGCGAAGA	CAGCTTGAGCGTCTGGATCT	human
FN1	CGGTGGCTGTCAGTCAAAG	AAACCTCGGCTTCCTCCATAA	human
Vimentin	ACTTTGCCGTTGAAGCTGCTA	AAATCTATCTTGCGCTCCTGA	human
Nanog	GCTGGTTGCCTCATGTTATTATGC	CCATGGAGGAAGGAAGAGGAGAGA	human
OCT4	TTTTGGTACCCCAGGCTATG	GCAGGCACCTCAGTTTGAAT	human
Snail3	AAATCA ATGGTGCCTGCTCT	GGCTGTCTTTGAGGGGTA	human
DSC1	TGATGGAGAACTCGTTGGGTC	CCTGGCCCACTTATGGAATAAAA	human
DSC2	TGTACTCGTCCTGTAGATCGTG	AGTGCCCACTCTGCAATTTTC	human
DSC3	TTCTCAGGCGTGCCAAGAG	ACTCCACGTCCACTTATTGAGTA	human
DSG1	AACCCAATCGCCAAAATTCACT	ACCTCTCGATCAACTATGGATGT	human
DSG2	CTAACAGGTTACGCTTTGGATGC	GTGAACACTGGTTCGTTGTCAT	human
DSG3	GCAAAAACGTGAATGGGTGAAA	TCCAGAGATTCGGTAGGTGATT	human
PKP1	GACCAGGACAACTCCACGTT	CTGCTGGTGGTCCCATGTT	human
PKP2	GTGGGCAACGGAAATCTTCAC	CCAGCCTTTAGCATGTCATAGG	human
PKP3	GGCCGACTATGACACACTCTC	CTCGGGGAAACCTCAGTGG	human
PG	TCGCCATCTTCAAGTCGGG	AGGGGCACCATCTTTTGCAG	human
DSP	TTTGGGCAGTAGCATGGGC	CCATCTTGGGTATTCTCTTGCCT	human
CLDN1	CCCTATGACCCCAGTCAATG	GTTTTGGATAGGGCCTTGGT	human
OCLN	ATGGCAAAGTGAATGACAAGCGG	CTGTAACGAGGCTGCCTGAAGT	human
MMP9	GGGACGCAGACATCGTCATC	TCGTCATCGTCGAAATGGGC	human
MMP14	GCAGAAGTTTTACGGCTTGCAA	CCTTCGAACATTGGCCTTGAT	human
MMP2	ATAACCTGGATGCCGTCGT	AGGCACCCTTGAAGAAGTAGC	human
PCNA	TCCTCCTTCCCGCCTGCCTGTAGC	CGCGTTATCTTCGGCCCTTAGTGTA	human
KI67	TGAAGATGCAGCTGACTCTG	AGCACTCTGTAGGGTCGAG	human
B-actin	TGGACATCCGCAAAGACCTG	GGGTGTAACGCAACTAAGTCAT	human

1311